POLITECNICO DI MILANO

Facoltà di Ingegneria Industriale e dell'Informazione

Corso di Laurea Magistrale in Ingegneria Fisica

Development of a GUI-based scientific software for the analysis of resonant inelastic X-ray scattering data acquired with 2D detectors

Relatore: Prof. Giacomo Claudio GHIRINGHELLI
Correlatore: Dott. Kurt KUMMER

Tesi di Laurea di:
Annalisa TAMBORRINO
Matr. 820020

a.a. 2015 - 2016

To my family...

Abstract

Resonant Inelastic X-ray Scattering (RIXS) is a "photon in-photon out" spectroscopic technique that probes elementary excitations in complex materials by measuring their energy, momentum and polarization dependence, with bulk sensitivity and chemical selectivity. Due to its unique features, RIXS has become one of the most innovative and powerful tools for the investigation of the magnetic and electronic structure of the systems under study. For this reason, several dedicated instruments have been built in many synchrotron facilities all over the world, exploiting the availability of high-brilliance X-ray radiation. During the last years, the instrumentation has achieved a great development, showing a continuously increasing energy resolution and improved sample position control. In fact, a new generation RIXS spectrometer for soft X-rays, called ERIXS, is now fully operative on the new ID32 Beamline at ESRF, in Grenoble. It has been designed and built by the group of Politecnico di Milano lead by prof. Giacomo Ghiringhelli and prof. Lucio Braicovich, jointly with the staff members of ID32. The group has previously designed the spectrometer AXES at the ID08 Beamline of the ESRF and SAXES at the ADDRESS Beamline of the SLS, giving a great contribution to the success of RIXS with soft X-rays. The application of RIXS in this energy range allows the study of the properties of transition

elements and rare earth compounds, but the energy resolution has always been a limiting factor for a full characterization and interpretation of the experimental results. This is one of the reasons that led to the construction of a high resolution spectrometer. In effect, ERIXS features unprecedented key figures that have been achieved through an extreme optimization of the components of both the Beamline and the spectrometer. The optical layout of a RIXS spectrometer is very simple: the radiation coming from the Beamline goes to the sample and the scattered beam is dispersed by a diffraction grating, that separates the different energy components and focusses them onto a 2D position sensitive detector. Data analysis software is needed to convert these 2D images into energy loss spectra. The image on the detector is composed of isoenergetic lines along one direction and the energy dispersion direction perpendicular to these lines. The resulting RIXS spectrum can be obtained through an integration along these isoenergetic lines, which we call the Traditional (or Integrating) algorithm. In this context, the spatial resolution of the detector and the size of the charge cloud generated by the photons play a crucial role. For this reason, an innovative algorithm (Single Photon Counting, SPC) was developed in the past years, in order to obtain the photon impact position, through a calculation of the center of mass of a group of pixels containing the spots. These are the two algorithms currently in use at the Beamline to extract the spectrum from a raw image coming from the detector. The individual spectra extracted from each image then need further processing before they can be summed to the final RIXS spectrum which is usually obtained from several tens to a hundred individual spectra. In the framework of this thesis, a software was developed that is able to help with all these steps and the data analysis. In addition, some further tools were implemented to be able to determine parameters like the detector inclination or the pixel to energy conversion factor needed in the data analysis. The software comes with a graphical user interface (GUI) to make the RIXS data

analysis easier and more intuitive to the users. This represents an added value for the Beamline, considering that many users from all over the world carry out their experiments with ERIXS and the available time is limited, thus a simpler and faster way to analyze the data becomes a very useful tool, both during and after the beamtime. The software is called RIXSToolbox and has been developed under the guidance of Dr. Kurt Kummer, Scientist at ID32.

RIXSToolbox is written in Python, a high-level programming language, with a large standard library. This choice arises from the fact that it provides tools for many tasks but, most of all, it is completely free, thus it doesn't require any license. It is now available online for download. A full characterization of the software will be provided in this thesis, describing all the functionalities in a simple way, supported by the real illustrations of the corresponding interfaces.

The description will feature a step by step analysis on NiO real images acquired with ERIXS during the commissioning of the instrument. At the end, the resulting RIXS spectrum will be shown as the output of the last step of the procedure.

The choice of illustrating this result has the dual purpose of showing the effective functioning of the software and the enhancement introduced by the utilization of the new spectrometer.

NiO is a 3d transition-metal oxide and is classified as a strongly correlated electron system. These materials have received a great deal of attention over the years, because of their promising physical properties, but they are still far from being fully understood. RIXS is a suitable technique for the investigation of this type of materials.

The spectrum shown in the last part of this work confirms that the new high resolution spectrometer ERIXS allows to obtain a real improvement as it can be clearly seen by comparing it with the definition and resolution of the

spectral features in previous works. For the case of NiO, in fact, we will see that it is possible to distinguish the magnon peaks that otherwise would be partially covered by the elastic line.
To summarize, the first half of this thesis work will introduce the new ID32 Beamline, focusing on the RIXS branch that hosts the now full operative ERIXS spectrometer. While the second one is dedicated to the presentation of the RIXSToolbox software, that is the central topic of the work, showing an example of utilization on a recently measured NiO RIXS spectrum that will be discussed in the last part.

Abstract

Lo scattering anelastico risonante di raggi X (RIXS) è una tecnica spettroscopica "photon in-photon out" adatta a investigare le eccitazioni elementari in materiali complessi misurandone la dipendenza dall'energia, dal momento e dalla polarizzazione con sensibilità al bulk e selettività chimica. Per via delle sue caratteristiche uniche, il RIXS è diventato uno dei più innovativi e potenti strumenti per lo studio della struttura magnetica e elettronica dei sistemi in esame. Per questo motivo, sono stati costruiti vari strumenti dedicati in molti sincrotroni nel mondo, sfruttando la disponibilità dell'alta brillanza della luce di sincrotrone. Negli ultimi anni, la strumentazione ha raggiunto un grande sviluppo, mostrando un continuo miglioramento nella risoluzione in energia e nel controllo del posizionamento del campione. Infatti, uno spettrometro di nuova generazione dedicato a misure RIXS con raggi X soffici, chiamato ERIXS, è attualmente operativo sulla nuova Beamline ID32 all'ESRF di Grenoble. È stato progettato e costruito dal gruppo del Politecnico di Milano guidato dal prof. Giacomo Ghiringhelli e dal prof. Lucio Braicovich, insieme allo staff di ID32. Tale gruppo aveva precedentemente progettato lo spettrometro AXES sulla Beamline ID08 dell'ESRF e, in seguito, lo spettrometro SAXES sulla Beamline ADDRESS di SLS, offrendo un grande contributo al successo del RIXS con raggi X soffici. L'applicazione del RIXS

in questo range energetico permette lo studio delle proprietà dei composti di metalli di transizione e di terre rare, ma la risoluzione energetica è sempre stata il principale fattore limitante per una completa caratterizzazione e interpretazione dei risultati sperimentali. Questa è una delle ragioni che ha portato alla costruzione di uno spettrometro ad alta risoluzione. Infatti, ERIXS presenta delle caratteristiche mai raggiunte precedentemente e che sono state ottenute attraverso un'estrema ottimizzazione delle componenti della Beamline e dello spettrometro. La configurazione ottica di uno spettrometro RIXS è concettualmente semplice: la radiazione proveniente dalla Beamline incide sul campione e il fascio scatterato viene disperso da un reticolo di diffrazione, che separa le diverse componenti energetiche e le focalizza su un detector 2D sensibile alla posizione. Le immagini 2D provenienti dal detector devono essere analizzate mediante un software per essere convertite in uno spettro RIXS. Queste immagini sono composte da linee isoenergetiche lungo una direzione, mentre la direzione di dispersione dell'energia è perpendicolare a queste linee. Lo spettro risultante, può essere ottenuto attraverso un'integrazione lungo le linee isoenergetiche, usando il cosiddetto algoritmo Tradizionale (o di integrazione). In questo contesto, la risoluzione spaziale del detector e la dimensione della nuvola di carica generata dai fotoni giocano un ruolo cruciale. Per questo motivo, negli scorsi anni è stato sviluppato un algoritmo innovativo (Single Photon Counting), con l'obiettivo di ottenere la posizione di impatto del fotone attraverso il calcolo dei centri di massa dei gruppi di pixel contenenti gli spot. Questi sono i due algoritmi attualmente in uso sulla Beamline per estrarre lo spettro dall'immagine del detector. Gli spettri individuali devono essere successivamente processati prima di essere sommati per arrivare allo spettro finale, che in genere è ottenuto da diverse decine di spettri. Nel contesto di questo lavoro di tesi, è stato sviluppato un software che permette di effettuare le varie fasi di elaborazione e analisi dei dati. Inoltre, sono stati implementati dei tools per la determinazione di

alcuni parametri come l'inclinazione del detector o il fattore di conversione dai pixel alle energie necessario per l'analisi. Il software si presenta con una interfaccia grafica (Graphical User Interface, GUI) in modo da rendere l'analisi più facile e intuitiva agli users. Ciò rappresenta un valore aggiunto alla Beamline, considerando che molti users da tutto il mondo effettuano i loro esperimenti con ERIXS e il tempo disponibile per le misure è limitato. Di conseguenza, un modo più semplice e veloce per analizzare i dati diventa uno strumento davvero utile, sia durante che dopo il beamtime. Il software è denominato RIXSToolbox ed è stato creato sotto la guida del Dott. Kurt Kummer, scienziato della Beamline ID32.

RIXSToolbox è stato scritto in Python, un linguaggio di programmazione di alto livello. Questa scelta si è basata sul fatto che Python fornisce strumenti adatti a vari scopi e, soprattutto, è gratuito e pertanto non richiede alcuna licenza. Il software è ora disponibile online e pronto per il download. In questa tesi verrà fornita una completa caratterizzazione del software, descrivendo tutte le funzionalità in modo semplice, con il supporto delle illustrazioni delle corrispondenti interfacce.

La descrizione presenterà una analisi "step by step" fatta su immagini reali di NiO acquisite con ERIXS durante il commissioning dello strumento. Alla fine, verrà mostrato lo spettro RIXS risultante come output dell'ultimo step della procedura.

La scelta di presentare questo risultato ha il duplice scopo di mostrare l'effettivo funzionamento del software e il miglioramento introdotto dall'utilizzo del nuovo spettrometro.

NiO è un ossido di metallo di transizione 3d ed è classificato come sistema di elettroni fortemente correlati. Questi materiali hanno ricevuto una grande attenzione negli anni, per via delle loro proprietà fisiche promettenti, ma sono ancora lontani dall'essere completamente capiti. La tecnica RIXS è adatta all'investigazione di questo tipo di materiali.

Lo spettro mostrato nell'ultima parte di questo lavoro conferma che il nuovo spettrometro ad alta risoluzione, ERIXS, permette un effettivo miglioramento come può essere visto comparando la definizione e la risoluzione delle caratteristiche spettrali dei lavori precedenti. Nel caso del NiO, infatti, si potrà vedere che è ora possibile distinguere i picchi magnonici, che altrimenti sarebbero parzialmente coperti dal picco elastico.
In sintesi, la prima metà di questo lavoro di tesi sarà dedicata alla presentazione della nuova Beamline ID32, in particolare sulla sezione del RIXS che ospita il nuovo spettrometro ERIXS. La seconda parte è invece basata sulla caratterizzazione del software RIXSToolbox, che rappresenta l'argomento principale del lavoro, mostrandone un esempio di utilizzo su uno spettro RIXS del NiO recentemente misurato, che verrà discusso nell'ultima parte.

Contents

Abstract viii

Abstract xii

List of Figures xv

1 Resonant Inelastic X-ray scattering 1

1.1 The scattering process in RIXS 1

1.2 RIXS features 3

1.3 Excitations accessible to RIXS 5

2 Advances in instrumentation for soft-RIXS at ESRF 11

2.1 Introduction to synchrotron radiation and ESRF 12

2.2 ERIXS at the new ID32 Beamline 16

2.3 Data acquisition system: use of CCD detectors for soft X-rays 27

3 New data analysis software for RIXS 35

3.1 Data elaboration procedure: from raw images to the final spectrum 36

3.2 RIXSToolbox characterization 44

4 NiO as a case of interest for high resolution RIXS **57**

4.1 Strongly correlated electron systems 58

4.2 NiO atomic structure 59

5 Experimental results at Ni L_3-edge **65**

5.1 Experimental progress of the last decade 65

5.2 Recently measured NiO RIXS spectrum with ERIXS 69

6 Summary **75**

Appendix **77**

Acknowledgments **81**

Bibliography **85**

List of Figures

1.1 Scheme of the RIXS process 2
1.2 Different elementary excitations in condensed matter systems . 6
1.3 Magnon dispersions at the Cu L_3 -edge on La_2CuO_4 8
1.4 Energy scheme of Cu L_3 RIXS 9
1.5 Relative intensity of charge-transfer spectral weight in NiO compared to the whole RIXS spectrum 10

2.1 Typical schematic picture of a modern storage ring 12
2.2 Sketch of the storage ring 13
2.3 Schematic picture of radiation emission from a bending magnet 13
2.4 Schematic picture of radiation emission from an undulator and a wiggler 15
2.5 ESRF top view 16
2.6 Schematic view on ID32 Beamline at ESRF 16
2.7 Sketch of ID32 optical layout 17
2.8 Schematic picture of the Apple II undulator 18
2.9 The ERIXS spectrometer at ID32 at ESRF 20
2.10 Optical layout of a RIXS spectrometer 21

2.11 Typical image acquired by a CCD detector in a soft X-ray spectrometer . . . 22
2.12 Sketch of the improvement in the effective spatial resolution for an inclined CCD . . . 23
2.13 Sketch of the sample plate . . . 24
2.14 Plot of a true energy loss spectrum . . . 25
2.15 ERIXS spectra compared to those of SAXES . . . 26
2.16 MOS capacitor structure . . . 28
2.17 Band diagram of deep depletion regime . . . 29
2.18 Charge transfer between neighbouring pixels . . . 30
2.19 Reading mechanism in a CCD detector . . . 30
2.20 Comparison between a front and a thinned back-illuminated sensor . . . 32
2.21 Sketch of charge cloud splitting process . . . 33

3.1 Typical experimental spectral line . . . 38
3.2 Procedure to align the isoenergetic lines with the pixel rows . 40
3.3 NiO, Ni L_3 RIXS spectra recently measured with ERIXS . . . 43
3.4 Software main interface . . . 46
3.5 Slope Finder . . . 48
3.6 Generate Spectra . . . 50
3.7 Alignment and Sum . . . 52
3.8 Comparison with and without alignment . . . 53
3.9 Calibration coefficient . . . 54
3.10 Energy Calibration . . . 56

4.1 The density of states (DOS) of electrons in a dynamical mean-field solution of the Hubbard model. . . . 60
4.2 Schematic illustration of the spin structure in NiO . . . 61
4.3 Representation of the atomic model of NiO . . . 62

5.1 Experimental NiO L_3 RIXS spectra measured with AXES . . 66
5.2 Experimental NiO L_3 RIXS spectra measured with SAXES . . 68
5.3 Experimental NiO L_3 RIXS spectrum measured with ERIXS . 70
5.4 Comparison between experimental and theoretical NiO spectrum 72

1 Resonant Inelastic X-ray scattering

Resonant Inelastic X-ray Scattering (RIXS) is a powerful spectroscopic technique for studying the low-energy excitations of materials [1] [2] [3] [4] [5] [6]. In particular RIXS can access charge, magnetic, orbital and lattice excitations with energy and momentum resolution. This experimental technique has been known for at least 40 years, but only in the last 20 years RIXS has made remarkable progress. This is a direct result of the availability of high-brillance synchrotron X-ray radiation sources and of the improvements in instrumentation.
In this Chapter, RIXS will be introduced in general terms, describing the scattering process and highlighting the main characteristics that make this technique unique.

1.1 The scattering process in RIXS

Resonant Inelastic X-ray Scattering (RIXS) is an experimental technique based upon a second order process that involves two steps, as shown in Figure 1.1. An incoming X-ray photon of energy $\hbar\omega_i$, momentum k_i , polarization ϵ_i hits the sample and promotes a core electron to an empty state above the Fermi level, creating a core hole. This excited state is very

unstable, with a lifetime of $\sim$ 1 fs. After this time the system rapidly decays into a final state emitting another X-ray photon of energy $\hbar\omega_o$, momentum k_o and polarization ϵ_o generated by the recombination of the core hole with a valence electron.

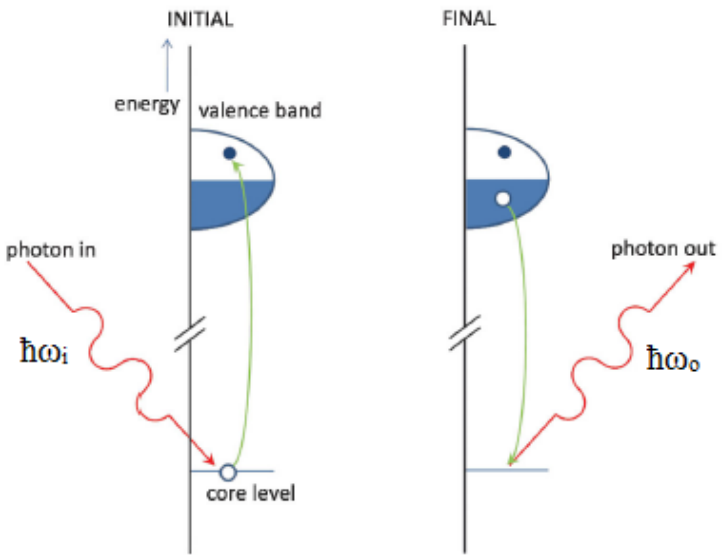

Figure 1.1: Scheme of the RIXS process: the incoming photon $\hbar\omega_i$ is absorbed and a core electron is promoted to an empty state above the Fermi level, creating an hole (left panel). Then the system decays because of the recombination between the core hole and a valence electron, emitting a photon of energy $\hbar\omega_o$ (right panel). Taken from [1].

Because of this interaction, two different situations may occur: if $\hbar\omega_o = \hbar\omega_i$ no energy is transferred to the sample at the end of the process. Elastic scattering has taken place, with no excitation of the system in its final state. Otherwise, if $\hbar\omega_o < \hbar\omega_i$ the system has undergone an excitation of energy $\hbar\omega_i - \hbar\omega_o$.

Because RIXS is a "photon in-photon out" technique, one can measure the

energy, momentum and polarization change of the scattered photon with respect to the incoming one. All these changes are transferred to intrinsic excitations of the material. Thus RIXS provides information about excitations that involve charge, spin and orbital degrees of freedom as well as lattice dynamics of the system. Because of the conservation laws for energy and momentum of the whole system, including both photon and scatterer before and after the scattering process, the energy and the momentum of the excitation in the system can be obtained by imposing that:

$$\hbar\omega_i = \hbar\omega_o + E^{exc} \tag{1.1}$$

$$\hbar\vec{k_i} = \hbar\vec{k_o} + \hbar\vec{q}^{exc} \tag{1.2}$$

where $\hbar\omega_i$ ($\hbar\omega_o$) is the energy of the ingoing (outgoing) photon and $\hbar\vec{k_i}$ ($\hbar\vec{k_o}$) is the corresponding momentum. A third conservation law applies to the angular momentum of the whole system and the polarization state of the ingoing (i) and outgoing (o) photons.
During a RIXS experiment, the parameters describing the incident photons are imposed by the photon source, while the scattered photons characteristics are measured using a RIXS spectrometer, whose features will be presented in Chapter 2.

1.2 RIXS features

Compared to other scattering techniques, RIXS has a number of unique features that makes it an unequalled technique for the study of elementary excitations in condensed matter physics.
First of all, no charge is added to or removed from the studied sample as a consequence of the scattering process: the overall charge neutrality of the system is thus preserved, unlike in other spectroscopic techniques, such as direct or inverse photoemission. In RIXS, no core-hole is present in the final

state and thus no electron-core hole interaction. This considerably eases the analysis and leads to sharp spectra not affected by life-time broadening.
The bulk sensitivity is another feature related to the use of X-rays: the penetration depth of resonant X-ray photons is material and scattering geometry dependent and for hard X-rays it is typically of the order of a few microns, while for soft X-rays is on the order of tens of nm. The incoming and outgoing photon can pass through several atomic layers, penetrating into the sample and probing the bulk of the material under study. This doesn't mean that only thick and massive samples can be used, in fact due to the relatively strong photon-matter interaction, RIXS is possible on very small volumes samples, thin films, surfaces and nano-objects.
Another profitable characteristic of RIXS is the element (or chemical) selectivity, based on the resonance with an absorption edge. As very well known, an absorption edge is a sharp discontinuity in the absorption spectrum of X-rays that occurs when the photon energy resonates with the excitation energy needed to promote a core electron above the Fermi level. Absorption edges represent then a signature for a given element. To measure a RIXS spectrum the incoming photon energy is tuned on purpose to a desired absorption edge, thus privileging the scattering from the corresponding element. In this respect RIXS allows one to excite selectively an element and study elementary excitations while "sitting" on that specific element. Moreover, since the chemical environment influences shape and energy of the absorption edge, one can discriminate between the same atomic species with different oxidation states or coordination symmetries, as long as the corresponding absorption resonances are sufficiently well separated in energy.
Finally, RIXS has q-resolution. Photons carry a momentum inversely proportional to their wavelenght (λ). This momentum is usually negligible for visible light, but it becomes not-negligible for X-rays where $\lambda \sim 1$ Å, compatible with the interatomic distance in solids. A sizable fraction of the first Brillouin Zone

(BZ) can thus be probed, contrarily to experiments using optical photons which are restricted to a region very close to the Γ point.
All these generic features of RIXS make it an attractive technique to study the intrinsic momentum-dependent, low-energy response of a material. Of course there are some practical limitations: the energy resolution of the instrumentation is the most critical one. As we shall see in Chapter 2, during the past years a lot of progress has been made on the instrumentation, resulting in a remarkable improvement of the resolution.
One of the most technologically advanced and best-performing instruments for RIXS experiments is the new ERIXS spectrometer at ID32 Beamline of the ESRF, Grenoble (FR). It works with a tunable energy range from 400 eV to 1600 eV, which corresponds to the soft X-ray range. The use of RIXS with soft X-rays has demonstrated to be very useful, because in this energy range there are the O K edge, the $L_{2,3}$ edges of 3d transition metals, for example copper, and the $M_{4,5}$ edges of rare earths.

1.3 Excitations accessible to RIXS

The elementary excitations of a material determine many of its physical properties: understanding the excitation spectrum of a system is a key to understand the system itself. A RIXS spectrum is the plot of the number of emitted photons versus the photon energy loss $\hbar\omega_i - \hbar\omega_o$: as shown in Figure 1.2, the elementary excitation spectrum in solids spans the range from plasmons and charge-transfer excitations at a few eV, determining for instance, optical properties, through excitons, *dd* excitations and magnons down to phonons at the meV scale. This versatility of RIXS is an advantage and at the same time a complicating factor, because different types of excitations will generally be present in a single RIXS spectrum. In this respect, strongly correlated electron materials, such as transition-metal oxides, are of special

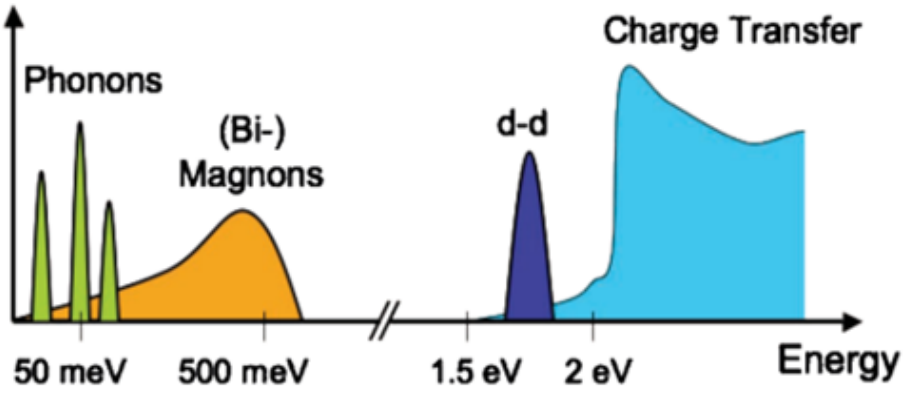

Figure 1.2: Different elementary excitations in condensed matter systems and their approximate energy scales in correlated electron materials such as transition-metal oxides. Taken from [1].

interest because the low-energy electronic properties are determined by high-energy electron-electron interactions (energy on the order of electron volts). Here, a general overview of elementary excitations is provided.

Charge-transfer excitations

In a condensed matter system, the charge transport phenomenon is determined by the energetics of moving electrons from one site to another. In a transition-metal oxide, there are two relevant energy scales for this process. The first one is the energy associated with the hopping of an electron from a ligand site to a metal site. This is known as the charge-transfer energy Δ, where $\Delta = E(d^{n+1}\underline{L}) - E(d^n)$, and $\underline{L}$ represents a hole on the ligand site. While the second one is the energy $U = E(d^{n+1}) + E(d^{n-1}) - 2E(d^n)$, associated with moving a d electron from one metal site to another. Strongly correlated insulators may be classified by which of these two energies is the larger [7]: if $U > \Delta$ the gap is of the charge-transfer type and the system is said to be a charge-transfer insulator, while if $U < \Delta$ the gap is controlled

by the *dd* Coulomb energy and the system is said to be a Mott-Hubbard insulator. Transition-metal oxide compounds, including cuprates, nickelates and manganites, are in the charge-transfer limit and this means that the lowest lying excitations across the optical gap are charge transfer excitations, thus these are of relevant importance in these materials.

Crystal-field and orbital excitations

In many strongly correlated systems, the valence electrons can occupy different sets of orbitals exhibiting an orbital degree of freedom that determines many physical properties of the solid under study. In many Mott insulators these orbital physics are governed by the crystal field: the J levels of the ion are split and the orbital ground state is uniquely determined by local, single-ion considerations. The orbital excitations from this ground state are transitions between the crystal-field levels. Crystal-field transitions between different d orbitals are called *dd* excitations. Such excitations are currently seen by RIXS and are now well understood. In other cases the crystal field doesn't split the levels of the outer shell very much, leaving an orbital (quasi-)degeneracy in the ground state. This local low-energy degree of freedom can couple to orbital degrees of freedom on neighboring sites by superexchange processes, and in this way collective orbital excitations can emerge. The quanta of these collective modes are called orbitons.

Magnetic excitations

When usual magnetic order sets in, the global spin rotation symmetry in the material is broken. Thus, characteristic collective magnetic excitations emerge and the resulting low-energy quasiparticles, the magnons, and the interactions between them, determine all low-temperature magnetic properties. Magnon energies can extend up to $\sim$0.3 eV (e.g. in cuprates) and their momenta up to 1 Å^{-1}. Recently magnon dispersions have been measured by

Braicovich *et al.* [8] for the first time with X-rays at the Cu L_3-edge on thin films of La_2CuO_4. In the past, studies of magnon dispersions have been a domain of inelastic neutron scattering. In Figure 1.3 a comparison between the

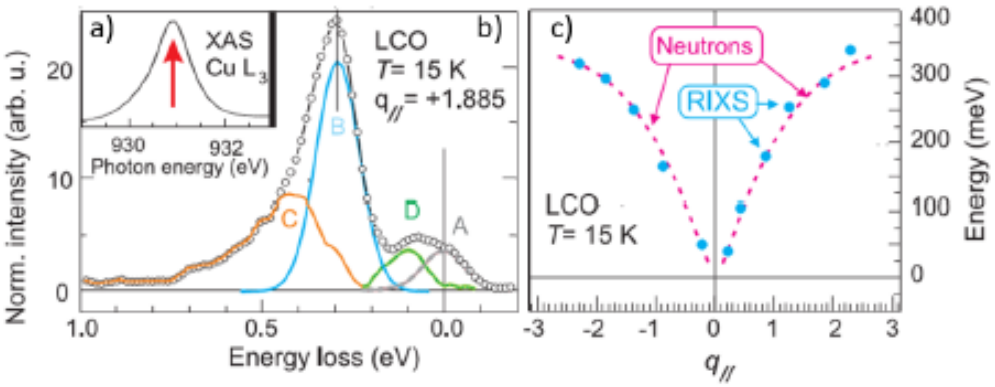

Figure 1.3: Panel (a): Cu L_3 absorption spectrum. Panel (b): decomposition of the LCO spectrum at $q_{//} = 1.85$ where elastic peak (A), single magnon (B), multiple magnons (C)and optical phonons (D) are shown. Panel (c) shows the single magnon dispersion obtained using RIXS and INS. Figure taken from [8].

results obtained with RIXS and inelastic neutron scattering (INS) is shown: they acquired a set of RIXS spectra with different in-plane momentum transfer and the resulting dispersion coincides with the one obtained with INS. This has been a remarkable result, also because with X-rays is possible to use very small volume samples, in contrast to neutron scattering techniques which usually require large single crystal.

Phonons

The quantized lattice vibration modes of a periodic solid are called phonons. Their energies are typically below 0.1 eV, an energy range which has become available only now. The loss features of single phonon excitations were resolved and investigated very recently at the Cu L_3-edge [8] and K edge [9].

In Figure 1.4, the RIXS process is summarized together with a typical RIXS spectrum of a cuprate. Each excitation visible in the spectrum is highlighted and connected to the transition from which it is generated.

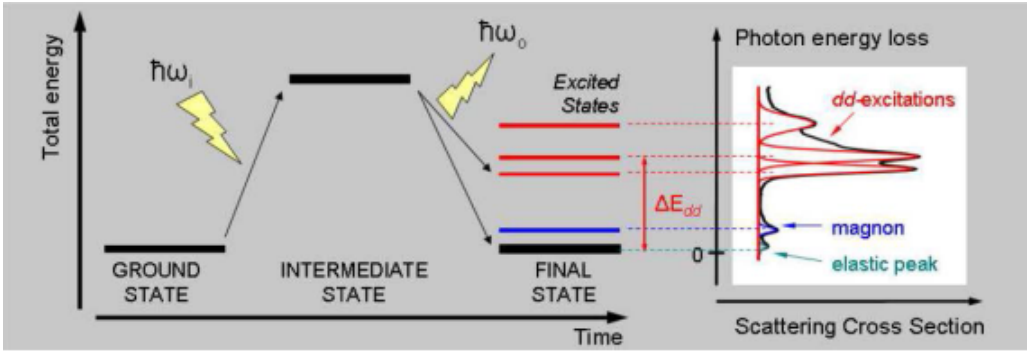

Figure 1.4: Energy scheme of Cu L_3 RIXS illustrated as a two-step process. The corrisponding typical RIXS spectrum of a cuprate is shown on the right side, where each excitation is evidenced. Figure reproduced from [10].

To carry out a RIXS experiment on a specific sample, the first choice is which absorption edge to work at. The most common edges for transition-metal compounds are the transition-metal L and K edges. After deciding upon an excitation edge, the next step is to choose the incident energy. Generally, during an experiment scans are made for a range of different energies. As a result, the intensity of the spectral features can strongly depend on the incoming photon energy. At an L edge, probing the main absorption line usually leads to transitions that are metal centered. When using energies in the satellite region above the main line, the charge-transfer features are emphasized. This can be seen in Figure 1.5, that shows a result for NiO obtained by Ghiringhelli *et al.* in 2005 [11]. It is clearly visible that at few eV above the absorption peak the inelastic processes are dominated by charge-transfer excitations.

Finally, it is also possible to study the polarization-dependence of RIXS features to gain further information about them. This requires the capability

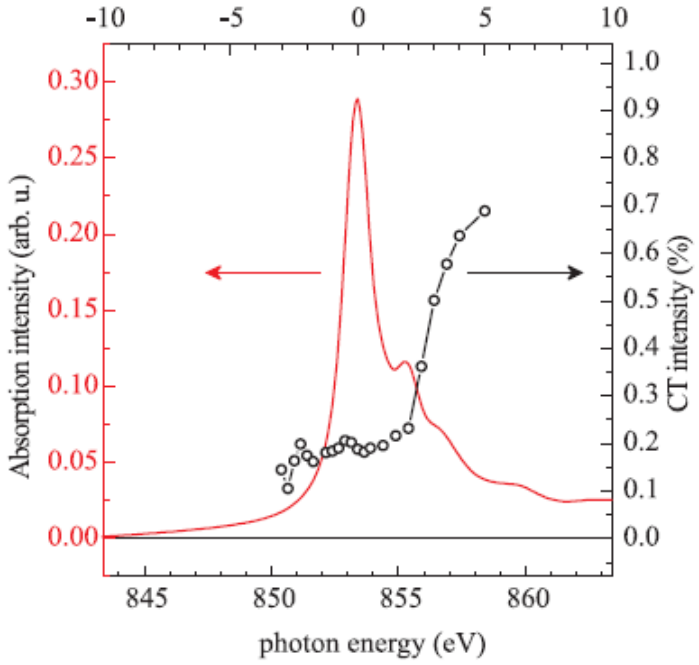

Figure 1.5: Relative intensity of charge-transfer spectral weight in NiO compared to the whole RIXS spectrum. The charge transfer process dominates for incident energies more than 4 eV above the peak in the absorption. Figure taken from [11].

to measure the outgoing polarization having fixed the incident one: this can be done with the use of a dedicated polarimeter.

After the general description of this powerful technique it's important to present the typical instrumentation required to carry out a RIXS experiment, focusing on the soft-RIXS instrument.

The next Chapter will be dedicated to this aspect, showing the implemented improvements and the currently available performances.

2

Advances in instrumentation for soft-RIXS at ESRF

The construction of third generation synchrotron sources and the design of advanced RIXS spectrometers have marked a turning point for the success of RIXS as an experimental technique. In fact, these advancements have allowed the overcoming of practical limitations due to the poor energy resolution and to the low photon flux provided by old generation synchrotrons. As a consequence of this remarkable progress, a new generation of advanced high resolution RIXS end stations is currently under construction in many facilities around the world. In this Chapter, after a general overview on the European Synchrotron Radiation Facility (ESRF) in Grenoble, the new soft-xray ID32 Beamline will be presented together with a description of its fully operational new generation RIXS spectrometer, called ERIXS. Its layout will be introduced in general terms focusing on the main principles and characteristics of the CCD detector, suitable for soft X-rays detection, currently in use at ID32. The CCD represents the most critical component because its spatial resolution is directly linked to the spectrum energy resolution [12]. Using analysis software on the acquired images, the RIXS spectrum is then obtained. In the framework of thesis, a user-friendly software with a graphical user interface (GUI) was developed to ease this last step of generation and analysis of RIXS

spectra.

2.1 Introduction to synchrotron radiation and ESRF

In the past decades, resonant inelastic X-ray scattering has made remarkable progress and this is a direct result of the availability of high-brilliance synchrotron X-ray radiation sources and of advanced photon detection instrumentation. It's thus important to introduce the synchrotron radiation characteristics and the European Synchrotron Radiation Facility in Grenoble (FR).

First of all, a synchrotron is an extremely powerful source of X-rays [13].

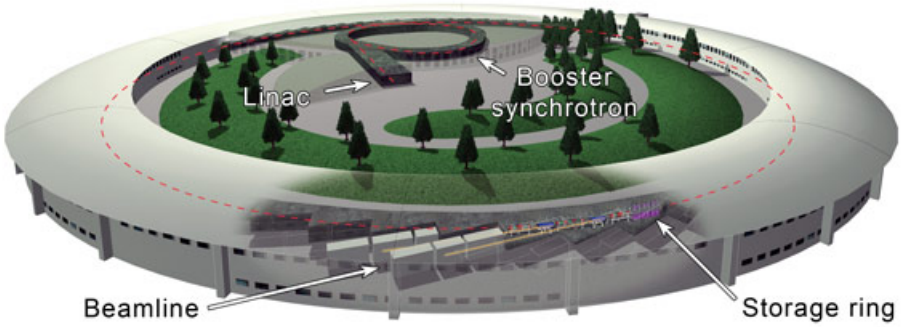

Figure 2.1: Typical schematic picture of a modern storage ring. Taken from [13].

It is based upon a main physical phenomenon: when an accelerated electron changes its direction, it emits energy; if the electron is moving fast enough, the emitted energy is at X-ray wavelengths.

The structure of a typical third generation radiation facility is sketched in Figure 2.1. Electrons are produced by an electron gun, accelerated by a linear accelerator, named linac, which at the ESRF is located inside the actual storage ring [14]. The electrons are then inserted in the booster ring, where

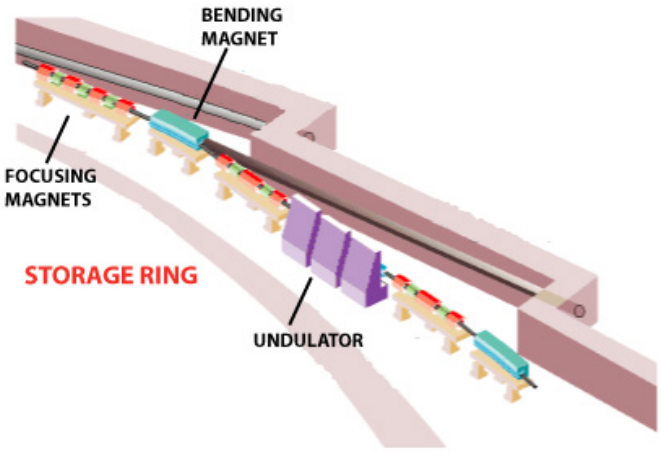

Figure 2.2: Sketch of the storage ring. Taken from [13].

they are further accelerated via electron-magnetic force. The electric fields need to be simultaneously increased with the gain of the electron beam energy, due to the increment of the relativistic mass, and this is the reason for the name "synchrotron". In the last step the electrons enter in the storage ring (Figure 2.2), where they keep circulating at relativistic velocity emitting the radiation directed toward the beamlines that surround the storage ring in the experimental hall. The curved trajectory is imposed to the electrons using

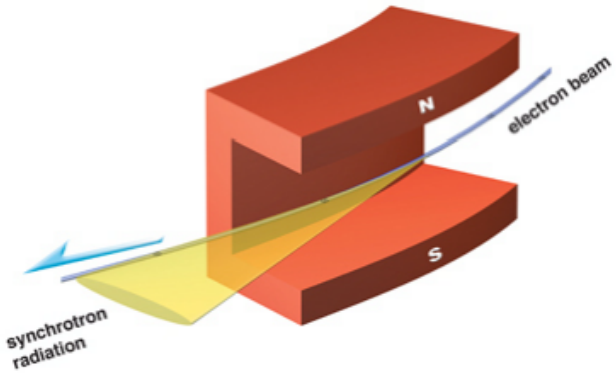

Figure 2.3: Schematic picture of radiation emission from a bending magnet.

magnetic field forces. Bending or dipole magnets (Figure 2.3) are used to curve the beam and thus to produce radiation tangential to the electrons orbit.

The second generation synchrotrons used these bending magnets to provide the X-ray photons to beamlines. The emitted radiation, due to relativistic effects, is directed tangential to the electron motion and has a very small divergence along the vertical direction, being confined within a small angle (usually less than 1 mrad) defined as $\theta \sim 1\ \gamma$, where γ is the Lorentz factor. Along the horizontal axis the beam divergence is bigger, being defined by the angle between vectors tangential to the electron trajectory before and after passing inside the magnet [15] [16]. Between two bending magnets, several quadrupole and sestupole magnets are used to focus the beam and correct the chromatic aberrations. These aberrations are due to errors in the focusing of the electrons characterized by a slightly different energy than the desired one. In order to avoid perturbations of the electrons trajectory inside the ring, the entire machine is kept in ultra high vacuum (10^{-9} to 10^{-11} mbar). A radio frequency (RF) system in the storage ring is used to supply electrons with the energy they lose (in the form of radiation) as a consequence of their centripetal acceleration.

Third generation machines differ from previous ones for the presence of insertion devices between bending magnets, that allow the production of radiation with higher brilliance, directionality and monochromaticity. Insertion devices consist of a periodic structure of magnetic dipoles, placed at specific distances, that produce a magnetic field that varies sinusoidally along the device's axis. Electrons passing through such a field undergo sinusoidal motion in the horizontal plane and this causes the emission of photons.

There are two kind of insertion devices (Figure 2.4). In wigglers, electron trajectory oscillations have angular deviation higher than 1 γ and this leads to negligible interference effect between light beams emitted along the device,

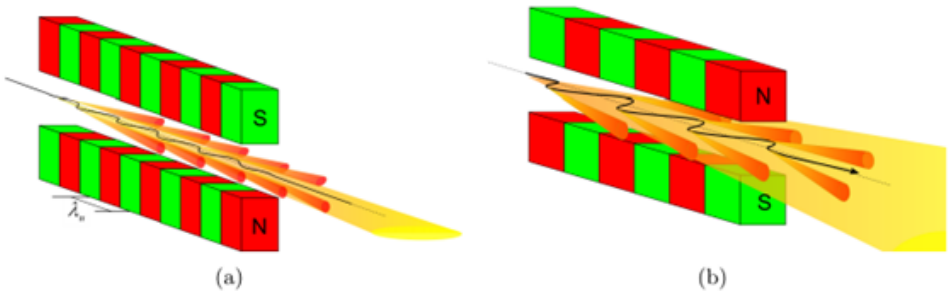

Figure 2.4: Schematic picture of radiation emission from an undulator (a) and a wiggler (b) insertion device.

resulting in an emission of radiation similar to the one of a bending magnet, but with higher brilliance and intensity. On the other hand, undulators are characterized by an electron trajectory confined within the angular aperture of the emitted radiation. This causes the radiation emitted in different points of the device to be coherent and interference effects become relevant. The resulting radiation spectrum is constituted by a series of discrete peaks of high intensity, whose energy can be modified by varying the magnetic field intensity. The radiation emitted by these devices is typically in the horizontal plane.

ESRF (Figure 2.5) has a storage ring of 844 meters circumference that serves 41 beamlines placed tangentially to it. The electron beam, of 6 GeV energy, is guided by 64 bending magnets and is focused by 320 quadrupoles and 224 sextupoles. All storage ring components are arranged in 16 superimposed cells with the same magnet distribution.

The current in the ring can reach 200 mA and has an average life up to 100 hours. In order to guarantee a constant and high flux of photons, every 12 hours the ring is refilled with new electrons.

The next section will present the ID32 Beamline of the ESRF, where my thesis project has been developed, giving a brief description of the instrumentation

Figure 2.5: ESRF top view. Taken from [13].

and the available techniques.

2.2 ERIXS at the new ID32 Beamline

ID32 is an intense source of polarized soft X-rays that is principally used to probe magnetism in a diverse range of systems and to study the electronic structure of materials.

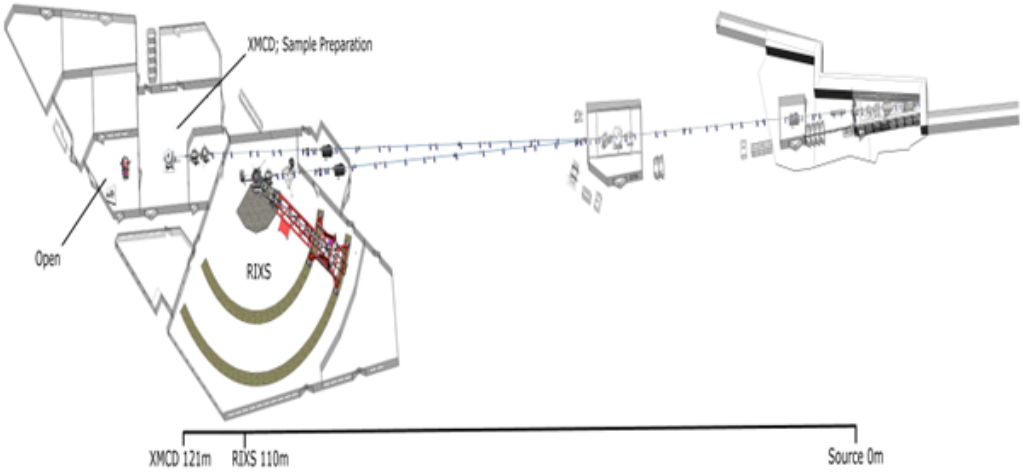

Figure 2.6: Schematic view on ID32 Beamline at ESRF.

The photon energy is tunable in the range of 0.4-1.6 keV making it ideal for studying the magnetic and electronic properties of 3d transition metals and rare earths since the L-edges (2p) and M-edges (3d) lie in this energy range. ID32 is the only soft X-ray beamline at the ESRF and was the second beamline to be inaugurated as part of the European Synchrotron's Phase I Upgrade. As depicted in Figure 2.6, it is made up of three end stations: one of them features an 11 meter spectrometer that provides unprecedented energy resolution. The instrument is able to rotate a full 100 degrees with the help of air pads which enable it to glide just above the marble slab below it. It is used primarily for investigating the magnetic and electronic properties of materials, including high temperature superconductors.
The second end-station, a UHV high magnetic field magnet allows to study the magnetic properties of materials, having potential importance in fields such as spintronics. Finally, a third "open" experiment area is for new user experiments, such as soft X-ray holography.
A sketch of the optical layout is depicted in Figure 2.7. The source of the

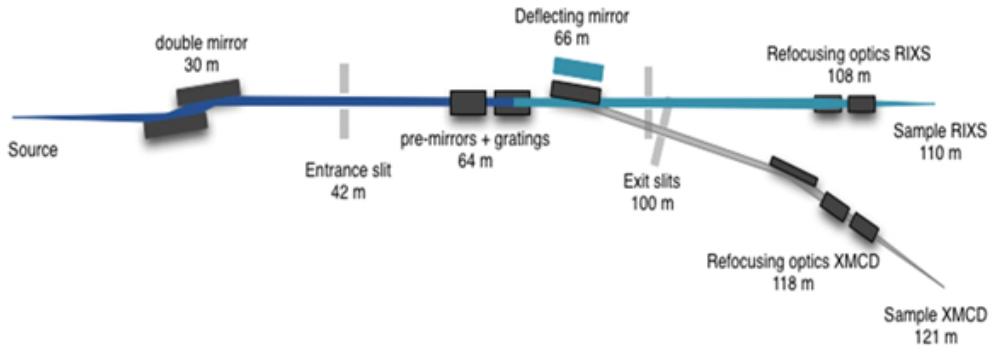

Figure 2.7: Sketch of ID32 optical layout.

Beamline is constituted by three APPLE II undulators (Figure 2.8) that provide 100 % controllable polarization, both linear and circular, of the emitted radiation, through 4 moveable permanent magnet arrays. X-rays are focused and filtered by a double mirror and enter the beamline monochro-

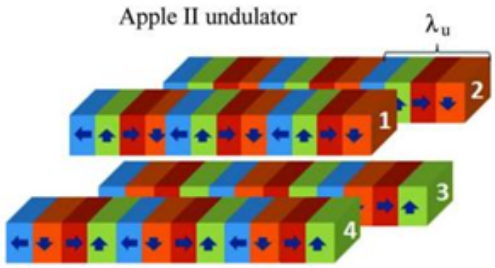

Figure 2.8: Schematic picture of the Apple II undulator.

mator through an entrance slit. The monochromator contains three gratings, one for the XMCD end station and two for the RIXS one. The entrance slit defines the position and the size of the source seen by the variable line spacing plane grating (VLS grating) which disperses photons with different energies along the vertical direction.

After the grating, a moving deflecting mirror allows to direct the beam either to the XMCD or to the RIXS end station. Then, the exit slit selects the energy beam range by spatially filtering the desired photons. The slit aperture defines the energy resolution of the beamline and must be chosen as a trade-off between resolution and photon flux.

From now on, we focus on the RIXS branch, being the main topic of my project.

To carry out a RIXS experiment a further refocusing of the X-ray beam on the sample is necessary. For this reason, a system based on a cylindrical sagital refocusing mirror and an elliptical bender is used for horizontal and vertical focusing onto the sample position respectively. The beam size for the RIXS branch is 4 x 60 μm^2 (FWHM). A liquid helium flow cryostat can provide temperatures down to 20K at the sample with all degrees of freedom preserved. The whole beamline is kept in ultra high vacuum conditions (UHV,

10^{-10} mbar) by ionic pumps. High vacuum (10^{-6} mbar) is necessary due to soft X-rays, that otherwise would be absorbed from air molecules. In addition to this, the requirement of UHV comes from the need to protect the beamline optical elements which otherwise could be damaged by the interaction with high energy photons and carbon atoms present in air. After the described path, the beam hits the sample and, for a RIXS experiment, photons scattered by the sample are analysed by the spectrometer. ID32 Beamline houses ERIXS (which stands for European-RIXS), the new RIXS spectrometer whose characteristics will be briefly described. ERIXS represents an evolution of AXES (which stands for Advanced X-ray Emission Spectrometer) that was installed and used at ID08 Beamline until this beamline was shutdown. AXES has been a leading instrument in the field of soft X-ray emission spectroscopy since 1994, when it was designed and then built by the group led by prof. L. Braicovich and prof. G. Ghiringhelli from Milan.
In 2005, prof. Ghiringhelli and prof. Braicovich started working on a project to build a similar RIXS instrument for the Swiss Light Source (SLS), based on the results and technical achievements obtained on ID08. They worked on the conceptual, optical and mechanical design and the construction of the instrument, called SAXES as Super AXES, property of the Paul Scherrer Institute and open to users at the ADRESS beamline since 2007 [17]. It proved to be a great success, opening new fields of research and attracting a lot of interest from different research groups and other facilities.

When the ESRF announced the first phase of its upgrade programme, prof. Ghiringhelli, together with Dr. Nick Brookes, scientist in charge of beamline ID08, proposed the conceptual and optical design project for a new instrument that would surpass the one installed at the SLS in terms of energy resolution. The project, which included several additional features and polarisation analysis, was received with much enthusiasm. This instrument, called ERIXS, stands proud today on the ESRF's ID32 beamline. As already

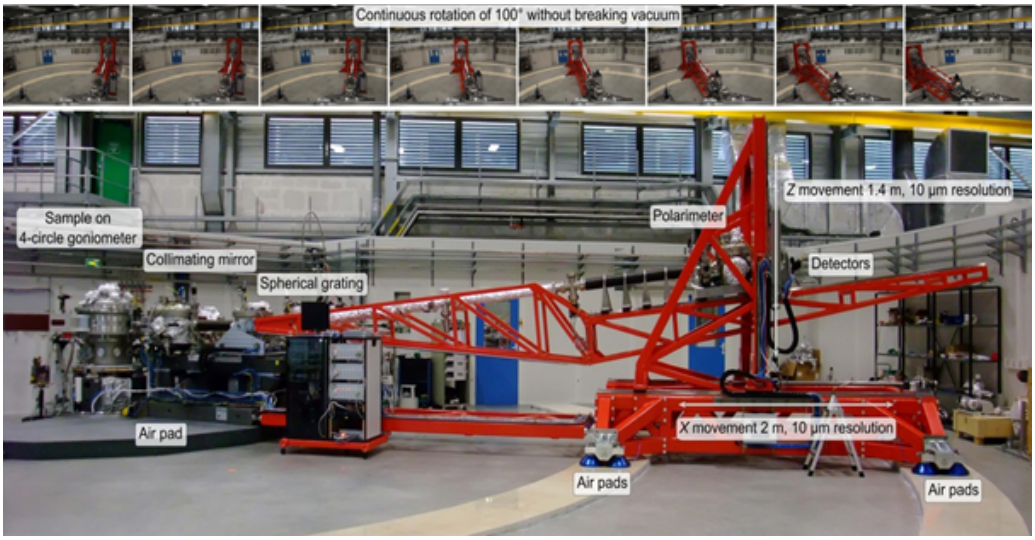

Figure 2.9: The ERIXS spectrometer at ID32 at ESRF.

mentioned, this spectrometer features an 11 m long scattering arm capable of rotating over 100° without breaking vacuum and a full in-vacuum 4-circle sample goniometer that allows a full control of the sample orientation.

Figure 2.9 shows the scheme of how the spectrometer works: part of the radiation emitted by the sample enters the spectrometer and hits at grazing incidence a spherical diffraction grating, that spatially separates different energy components of the beam and focus them onto a 2D position sensitive detector. The beam spot on the sample directly serves as the source for the spectrometer which therefore can work without an entrance slit. Before the grating the beam is collected and collimated by an elliptical mirror in order to increase the solid angle seen by the detector. According to the spectrometer design, the detector chosen for ERIXS is a commercial thinned back-illuminated CCD for soft X-rays (more informations about the detector will be provided in section 2.3) and, apart from the collimating mirror, the grating is the only optical element in the spectrometer. This simple scheme, as shown in Figure 2.10, was adopted in order to have an easy-to-use instrument and, above all, minimize all high order optical aberration thanks to a variable

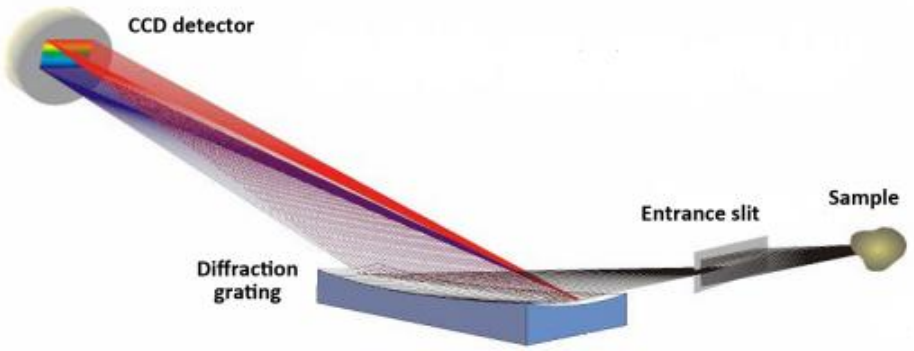

Figure 2.10: Optical layout of a RIXS spectrometer: the light coming from the sample hits on the VLS grating and is dispersed toward the detector. Reproduced from [18].

line spacing. Its average groove density varies along the grating which helps focussing the dispersed beam on the detector. The grooves disperse radiation along the vertical direction, deflecting at higher angles low energy photons, which thus will hit the detector in its upper region, while higher energy photons hit the detector surface in its lower part.

ERIXS has two exchangeable gratings that allow choosing between two different working mode: high efficiency (HE) or high resolution (HR). In the first case, the average groove density of the grating is a_0(HE)=1400 lines/mm, while for the second case is a_0(HR)= 2500 lines/mm. The HE grating has been used in the early stage of the commissioning, achieving 50 meV combined (spectrometer plus Beamline) BW, while the HR has been recently tested providing 35 meV FWHM, both at CuL_3-edge. The gratings are concave with a fixed radius of curvature, in order to focus all different energy components onto the CCD. The image acquired with the detector is thus constituted by isoenergetic lines that are approximately horizontal and their relative vertical positions correspond directly to their energy: the actual spectrum is obtained

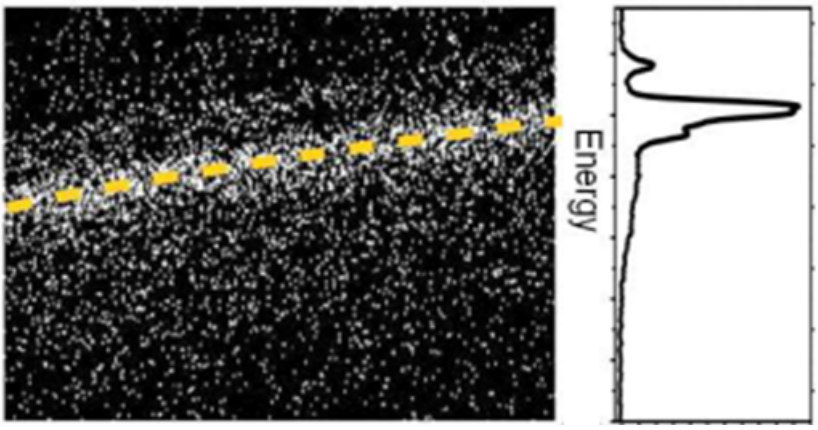

Figure 2.11: Typical image acquired by a CCD detector in a soft X-ray spectrometer; the integration along the direction indicated by the yellow line leads to the spectrum. Figure reproduced from [19].

by integrating along that direction, as depicted in Figure 2.11. Therefore the CCD positioning is crucial to select the desired photon energy range and thus the spectral window under study. The CCD surface should also be positioned on the grating focal plane, to avoid energy resolution losses. Another problem connected with the grating that can cause resolution losses is coma aberration. This effect is proportional to the square of the grating length used to focus the beam. To limit this area some masks could be placed before the grating reducing the lateral size of the illuminated region; this causes a loss in signal intensity and hence a trade off choice between intensity and resolution is again needed. The spatial resolution of the CCD detector determines the virtual exit slit of the spectrometer. The effective spatial resolution of modern CCD detectors is around 25 μm, irrespective of the pixel size, as a consequence of spots generated by X-ray photons hitting the detector, that involves some neighbouring pixels.

As it is depicted in Figure 2.12, two spots due to two photons hitting the CCD at different heights would overlap in case of detector perpendicular to the optical axis. In case of grazing incidence the same photon spots would

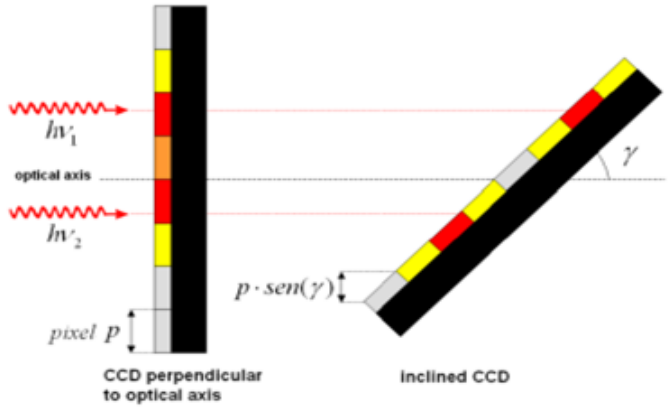

Figure 2.12: Sketch of the improvement in the effective spatial resolution for an inclined CCD [10]. The gain in spatial resolution is equal sen(y), where y is the angle between the detector surface and the optical axis of the spectrometer.

be spatially separated. In ERIXS the detector is inclined to a 30°angle, and this reduces the spatial resolution to around 6-7 μm. As a consequence of the inclination, the CCD surface is no more on the plane perpendicular to the optical axis on which the image is focused, and a defocusing problem could arise. However, this effect is fully compensated by the gain in spatial resolution.

Furthermore, two identical detectors are available for signal detection. The first one is positioned on the straight path of the scattered photons, as already explained. The second one collects the signal coming from a multilayer mirror based polarimeter that can be inserted in the path, intercepting a fraction of the beam. The measurement of both signals leads to a complete analysis of the scattered beam linear polarization.

To carry out an experiment, the samples are usually attached on a copper sample holder with silver paint, double-sided metallic adhesive tape or conductive glue (Figure 2.13); the holder is then mounted on a four-circle goniometer. It is necessary to have a conductive system in order to supply electrons to

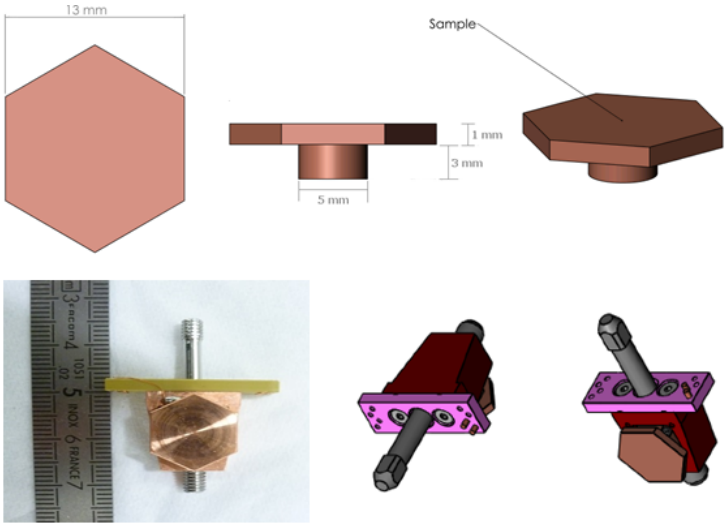

Figure 2.13: Sketch of the sample plate, which is mounted on specialised sample holder and thansferred in UHV to the goniometer by a screw system.

samples which lose charges when hit by X-rays due to photoemission. On the sample holder many samples can be mounted and this is useful to carry out different experiments without the need to warm up, transfer, and cool down samples. The goniometer allows samples to be moved in the three spatial directions as well as rotation around three axes in order to align the sample and to change the scattering vector in reciprocal space.

An important feature of a spectrometer is the resolving power, which depends on different experimental parameters.

First of all the finite source size brings to a spatial uncertainty on the beam path into the monochromator, that contributes to the energy resolution of the final spectrum. Another contribution to combined resolution is given by the already discussed spatial resolution of the detector. However this is enhanced by using it at grazing incidence. The last and most important element that influences the spectrometer resolution is the grating, with aberrations introduced by approximations in the shape and by errors in the actual realization of the optical element (as slope error). Coma aberrations are reduced with a

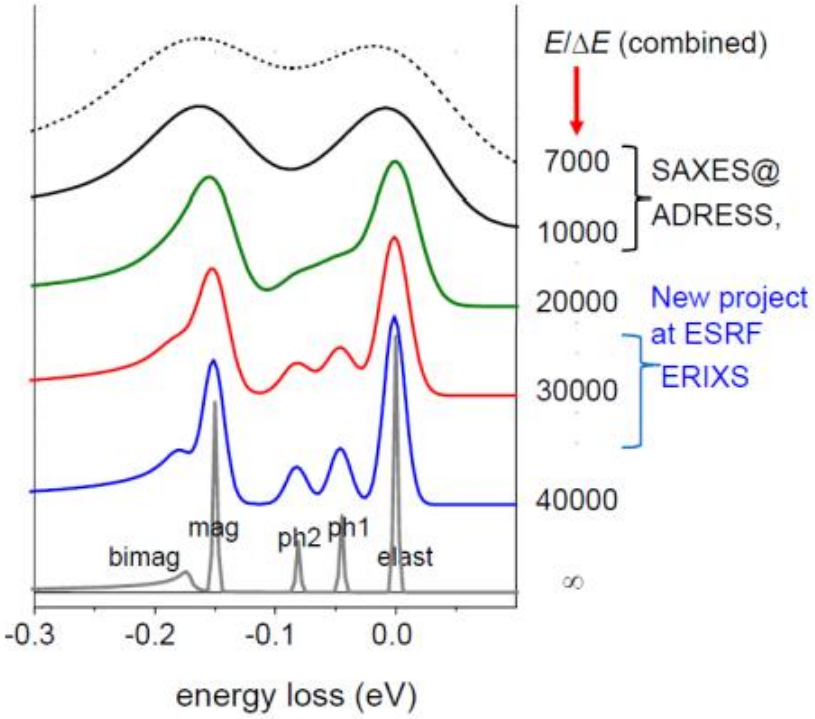

Figure 2.14: Plot of a true energy loss spectrum obtained with a RIXS spectrometer with increasing resolving power from top to bottom. Reproduced from [18].

mask that can be used to control the length of the footprint on the grating surface.

To consider the total resolution limit of the system for a RIXS experiment one has to consider also the contribution coming from the Beamline, i.e. the linewidth of the monochromator. The actual combined resolving power of Beamline and spectrometer is in fact given by the quadratic sum of all the listed contributions:

$$\Delta E_{tot} = \sqrt{\Delta E_{BL}^2 + \Delta E_{SPEC}^2} \tag{2.1}$$

The combined resolving power of ERIXS is 30000.

Figure 2.14 shows how a true energy loss spectrum is affected by the acquisition system depending on its resolution and highlights the fact that ERIXS

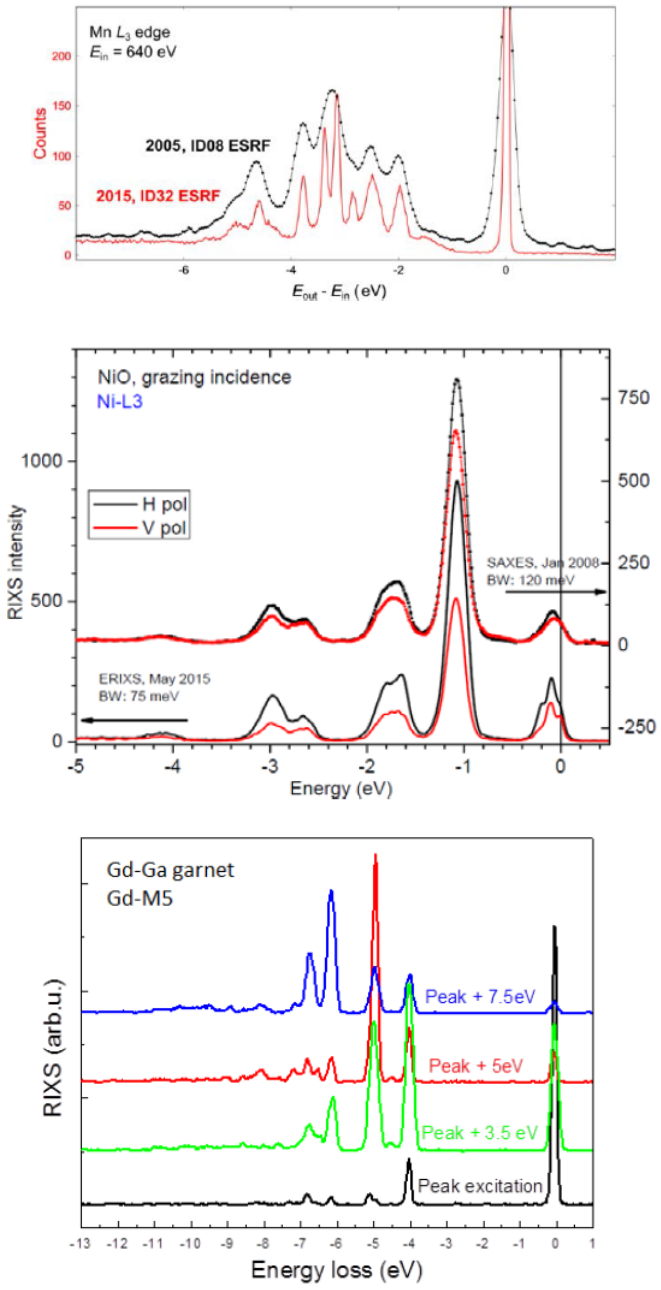

Figure 2.15: RIXS spectra measured with ERIXS. From top to bottom: MnO Mn-L_3 RIXS compared to previous AXES spectra [20] demonstrating better performances; NiO Ni-L_3 RIXS compared to SAXES [21] showing rich *dd*-excitations and a double magnetic peak; $Gd_3Ga_5O_{12}$ garnet Gd-M_5 RIXS and detuning effects, showing sharp *ff*-excitations compared to [22]. Reproduced from [23].

allows to resolve smaller spectral features that otherwise would not be seen, representing a big improvement with respect to SAXES.
During the April-May 2015 commissioning, some RIXS measurements at different edges were performed: Ni-L_3, Mn-L_3, Ti-L_3, Ce-M_5, Gd-M_5, Eu-M_5. In figure 2.15 there are three of these acquired spectra, showing the comparison with those measured with SAXES.
As we shall see in the next section, the high resolution that can be achieved with this new instrumentation can be limited by the detectors characteristics. In order to overcome this problem, an innovative algorithm for images acquisition has been developed in the last years by Andrea Amorese [12] [19], Phd student at ID32 and it will be discussed in Chapter 3.

2.3 Data acquisition system: use of CCD detectors for soft X-rays

The Charge Coupled Device (CCD) is an image sensor which allows the conversion of the incoming light into an electronic signal through the presence of a matrix of equal elements (pixels) that collect an electrical charge proportional to the photons flux hitting the surface. Each pixel is represented by a Metal-Oxide-Semiconductor Heterojunction (MOS) which is composed of three layers: a p-doped silicon substrate, a silicon oxide (SiO_2) insulating layer and a metal contact called gate, as depicted in Figure 2.16. As a consequence of a voltage application V_G to the gate, the electronic properties change accordingly and thus different working regimes can be identified. In order to have a charge accumulation, the MOS has to be out of equilibrium, in deep-depletion regime. What happens is that, starting from the accumulation regime, V_G is rapidly switched to a voltage higher than a characteristic threshold V_T and this leads to a band bending as sketched in

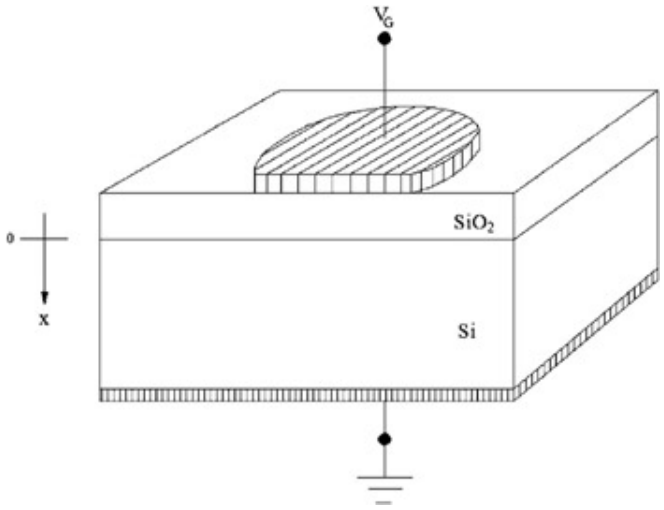

Figure 2.16: MOS capacitor structure.

Figure 2.17, where E_C and E_V are the conduction and valence band while F_n and F_p represent the Fermi quasi-levels of holes and electrons. The Si-SiO_2 interface is immediately depleted of electrons, which are minority carriers in p-doped silicon, leaving an almost zero concentration near the oxide. In order to restore the equilibrium of Fermi quasi-levels an accumulation of electrons at the interface is necessary and two different processes can occur: drift-diffusion of electrons from the bulk and electron-hole pair generation.

The latter mechanism is the one that allows the use of CCD detectors as image sensors. A photon incident on the substrate, with energy higher than the Silicon Energy Gap (the gap of Si is 1.11 eV at 300 K), can be absorbed and excites an electron from the valence to the conduction band. The electron-hole pair is separated by the electric field within the depleted region and cannot recombine, thus electron accumulation at the interface is possible. In order to have a direct proportion between the charge accumulated under each pixel and the incoming photon flux, it's important that the contributions due to thermal generation and electron diffusion from the bulk are negligible. This is ensured by using high pure silicon crystals and working at low temperature. The accumulated charge under each pixel has to be

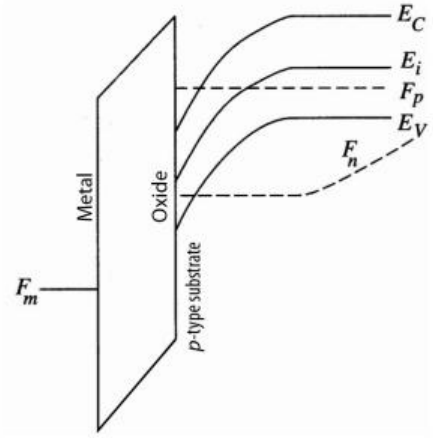

Figure 2.17: Band diagram of deep depletion regime.

measured and converted to an electronic signal: this is done by moving charges from pixel to pixel towards one end of the device, where a serial register is placed and connected to an analog to digital converter. The mechanism just mentioned is called Charge Coupling and allows the charge transfer between neighbouring pixels according to their applied V_G. A simple representation is sketched in Figure 2.18 where we consider two adjacent MOS capacitors. Starting from a situation in which the gate voltage of the left one is $V_{G1} > V_T$, charge accumulation at the silicon-oxide interface is thus allowed, while the second one is kept with $V_{G2} < V_T$ in order to prevent it. As can be seen, charges are confined in a potential well under the left one due to the different applied gate voltages. If V_{G2} is brought to V_{G1} value, the previous barrier is no longer present, thus the charge can flow toward the second capacitor, resulting in an equal distribution within the two MOS. Then the gate voltage of the left one is lowered below V_T, reversing the initial situation, allowing the confinement of the charge within the right pixel. The described steps are repeated consequentially between the other contiguous pixels.
In order to reach the converter, the charge of the bottom pixel row is moved to a serial shift register and all the other charges are consequently shifted one

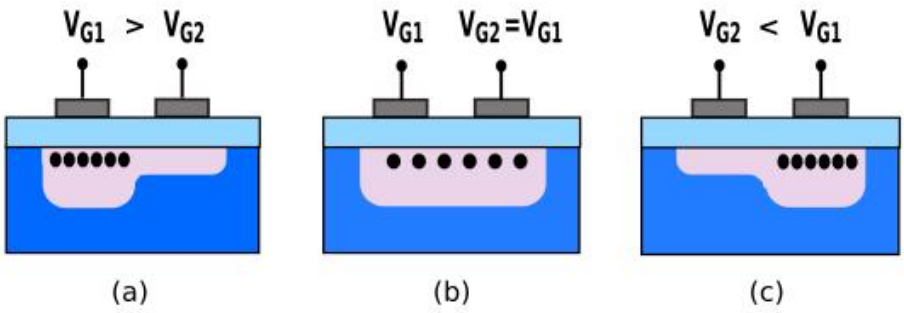

Figure 2.18: Charge transfer between neighbouring pixels.

row down (Figure 2.19). Each capacitor in the row transfers its content to the neighbouring pixel and the last one gives its content to a charge amplifier which performs the signal conversion and the output is stored in memory. Then the process is repeated for every shifted row until all the pixels signal of the CCD matrix have been digitalized.

The readout process can be critical for measurement, as for example in RIXS spectra, in which the duty cycle, defined as the ratio of the exposure time over the total time necessary to acquire an image, is essential. This means that the readout speed is a crucial parameter. A high duty cycle is linked to the efficiency and allows faster data collection. A low duty cycle, instead, could

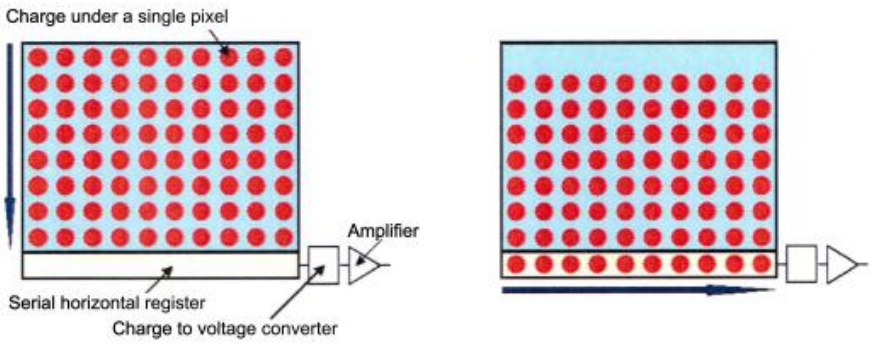

Figure 2.19: Reading mechanism in a CCD detector.

also lead to image modification, because if the readout time was much longer than the exposure time, many charges would be generated during the reading process when the electrons are shifted and this means that new photons hitting the detector before the end of the acquisition would be assigned to the wrong pixel. In order to overcome this problem a shutter can be used, stopping the beam while reading the pixel matrix. Therefore, the exposure time should not be too short with respect to the readout time, otherwise there would be a loss in duty cycle, but nevertheless it has to guarantee a low photon density on the image, which is a requirement for the processing algorithms.

The above explained CCD structure requires some particular features in order to extend its utilization in the soft X-ray range: the thinned back illuminated CCDs.

In the case of a frontside illuminated CCD, photons have to cross a "dead layer" of several thousand angström̈s, constituted by the gates and the silica layer of the MOS structure, before reaching the active part of the CCD where they generate photoelectrons that can be collected in a potential well. The absorption length of visible radiation is great enough, compared to the thickness of the dead layer, to make the decrease in sensitivity negligible. This is not the case in the soft X-ray range, where a significant fraction of the incident radiation is absorbed before it reaches the photosensitive part of the CCD. The search for optimized detection efficiency has led to a new structure of sensors: the thinned back-illuminated CCDs [24], i.e. a device illuminated from the substrate layer, whose thickness is suitably optimized in order to well match the X-ray absorption length. In Figure 2.20 both the structures are represented.

The exposition of the CCD to a uniform X-ray photon source with a low photon flux allows to distinguish individual charge clouds which correspond to single photon events. This is the working condition suitable for the application

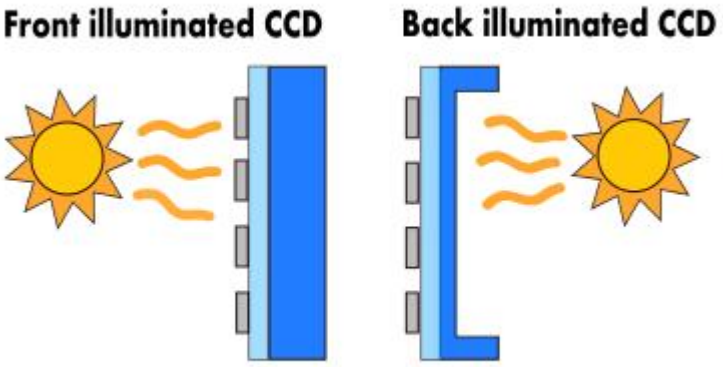

Figure 2.20: Comparison between a front and a thinned back-illuminated sensor.

of single photon counting algorithm, as it can be seen in the following Chapter. What happens is that this clouds are split among several pixels and this makes the spatial resolution of the detector worse (which is almost independent of the pixel size if this is smaller than the charge cloud). The charge cloud splitting process, depicted in Figure 2.21, is mainly due to the fact that if we consider an incoming X-ray photon with an energy larger than the energy gap of silicon, the photo-ionized electrons thermalise by scattering and produce an avalanche of secondary ionizations, leading to an approximately spherical charge cloud, smaller than the pixel area. Then, the cloud propagates to the pixel interface, while laterally diffusing [25]. This depends on the local electric field strength in the region where the cloud is generated: the stronger field at the interface causes compact clouds, while photons absorbed far away from the oxide result in bigger clouds. Furthermore, this charge cloud is split into charge packets by the pixel matrix. The number of pixels involved depends on the cloud and the pixel size and also on the impact position, because if the photon hits on the border between two adjacent pixels the probability of a split event is higher. The detector used at ID32 Beamline is a Princeton PI-SX 2048 CCD, which is a back-illuminated sensor optimized for X-ray

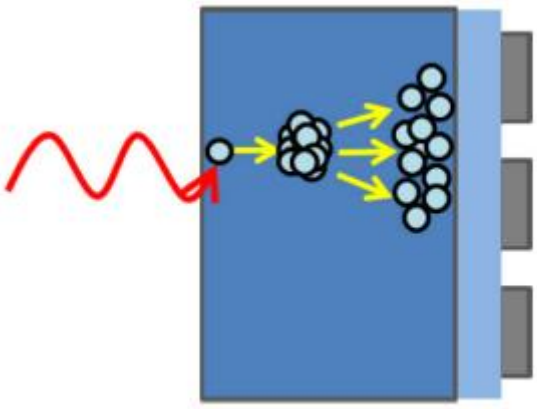

Figure 2.21: Sketch of charge cloud splitting process: an incoming photon hits the detector generating a charge cloud which split among several pixels.

detection. It exhibits a quantum efficiency (defined as the ratio between the number of revealed photons and the number of the incoming photons) higher than 65 % in the whole energy range of interest for RIXS application, with its maximum (QE=85%) at the Copper L_3 edge at around 930 eV.
The CCD is arranged in a matrix of 2048×2048 pixels, whose area is 13.5×13.5 μm^2.
During the experiments, the detector must be cooled down with liquid nitrogen to the temperature of -110°C in order to reduce electron accumulation due to thermal generation and diffusion that contributes to dark current and can saturate the pixel during long exposures.
As already explained, after exposition, the charge of the pixels is read and converted to a voltage signal and then, a constant offset is added to this signal to ensure that the output is not negative and it is finally digitalized by a 16 bit A/D converter. Two different conversion speeds are available: the low noise mode which works at 100 kHz and the high speed mode at 1 MHz (gaining a factor 10 in the duty cycle but with an higher noise and

non-uniform background problems). During an acquisition process, the main contributions to the total noise that affects the final data are the dark current and the A/D readout noise, as it can be seen by the following formula:

$$n = \sqrt{d_{rms}^2 + r_{rms}^2} \tag{2.2}$$

where n is the total noise, d is the dark current, r is the readout noise and the root main square value is expressed in electrons per pixel. The dark current is due to accumulated charges which are not generated by photo-ionization and this contribution is around 12 electron/h per pixel, at low temperature conditions. Instead the readout noise, due to the conversion electronics, depends on the chosen reading mode, being 4 electrons rms at 100 kHz and 10 electrons rms at 1 MHz (the noise values are the results of the last performed test).

After the description of the detector used at ID32 Beamline, it's important to know how the acquired raw images are elaborated in order to get the final spectrum. In the following Chapter an explanation of the available algorithms will be provided, together with the complete data analysis procedure.

3

New data analysis software for RIXS

This Chapter aims to present the main topic of my thesis project during my traineeship at ESRF: the development of a new data analysis software for the RIXS end station at ID32 Beamline. It has been done under the guidance of Dr. Kurt Kummer, ID32 Beamline Scientist, and the main goal was to automate and improve all the processes involved in data analysis in order to offer a simpler, faster and more intuitive way to perform all the required steps. Before presenting the software, it's important to introduce the necessary steps in the data analysis to obtain the final spectra, starting from raw images coming from the CCD detector, as already explained in the previous Chapter. The first step is the generation of a spectrum for every acquired image. This can be done through two algorithms currently in use at the Beamline: Traditional algorithm and Single Photon Counting algorithm.

The traditional algorithm is the simplest approach and corresponds to integration of the CCD counts along isoenergetic lines. Raw images are only pre-processed by subtracting a mean background and filtering out the single pixels whose intensity is inconsistent with the experimental process. This method gives good results but it has a main drawback: the resolution is limited by the charge cloud size (as explained in Chapter 2). This can be overcome by using the Single Photon Counting Algorithm. In fact, if the

impinging rate on the sensor is low, clouds generated by single photons can be identified and analyzed individually. The center of mass of each photon spot is calculated and localized on the pixel matrix and this allows a great resolution enhancement, breaking the pixel size limit.
During the experiment, many acquisitions in the same conditions are performed in order to have better statistics on the spectrum. The next step is then to compute possible shifts between the spectra and then sum all these spectra. After that, since the spectra are still only given vs pixels indexes, it's necessary to convert them into energies. As a result, the energy loss spectrum is complete and ready for any further analysis. This entire procedure, from the spectra generation to their alignment and their sum is now available using the RixsToolBox software, that can be downloaded from [26] , whose main features will be presented in the second section of this Chapter.

3.1 Data elaboration procedure: from raw images to the final spectrum

During a RIXS experiment, the scattered beam coming from the sample hits the VLS grating and is thus dispersed in energy in the vertical direction and focused on the CCD surface. Therefore the image acquired by the detector consists in approximately horizontal isoenergetic lines parallel among each other. As a consequence, the energy of the photons directly corresponds to the vertical positions on the CCD. These images need to be elaborated in order to obtain the corresponding energy loss spectra. Two algorithms are currently available at the Beamline: Traditional and Single Photon Counting algorithm.

Traditional algorithm

The traditional algorithm represents the simplest approach to the problem and consists in three main steps :

- Image filtering
- Conversion from ADU to photons
- Spectrum integration

The image filtering is the first step. There is an offset on the image due to the A/D converter that adds an offset to the signal in order to overcome possible zero line problems during conversion: this constitutes a background on the image and needs to be removed because it overlaps the true intensity. It is possible to calculate the amount of this offset evaluating the mean value of pixel intensities in a region of the image not exposed to X-rays. After that, this value is subtracted to the total image.
Then, two thresholds are used in order to get rid of contributions that are not part of the true spectrum:

- A low threshold (LT) sets to zero all the pixels with a signal below its value because, after the offset subtraction, pixels not involved in charge accumulation can still present some small or negative value due to noise contributions.
- A high threshold (HT) sets to zero all the pixels with a signal above its value and it happens when a pixel has an intensity that is too high to be compatible to X-rays. This event is typically ascribed to cosmic rays, that reach energies in the MeV range.

The choice of the high threshold value may be difficult with a high photon flux, because multiple events can occur generating high intensity in some

pixels. A too low value might remove a true signal, a too high value might not efficiently remove cosmic rays. It is also important to take into account that cosmic rays generate very big spots involving many pixels, where although the central ones exceed the HT value, the tails are usually below it. The solution is to work with a short exposure time as the number of cosmic rays events change proportionally to it. In Figure 3.1 a typical spectral line on the image is shown before (left) and after (right) filtering.

The second step is to convert the pixel intensity from ADU (Analog to

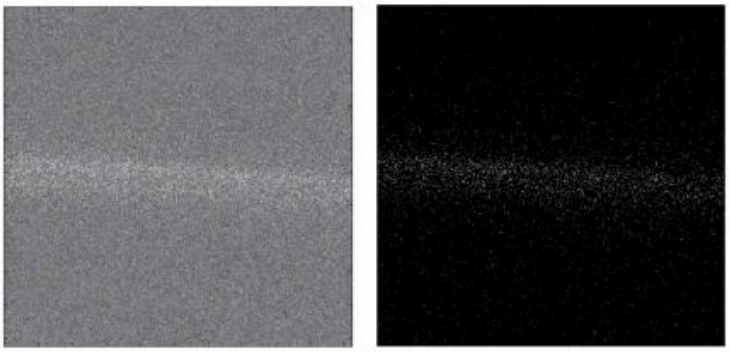

Figure 3.1: Typical experimental spectral line before (left) and after (right) filtering.

Digital Unit) to photons, using the following relation:

$$I[photons] = \frac{3.6 \cdot 2.5}{Photon\ energy[eV]} \cdot I[ADU] \tag{3.1}$$

where 2.5 is the converter gain electrons/ADU (experimentally evaluated) and 3.6 eV is the average energy needed to generate an electron-hole pair in silicon. All the energy of the absorbed photon is assumed to be converted into electrons, forming the charge cloud.

The last step is to perform the integration along the isoenergetic lines, in order to obtain the spectrum. The detector was mounted such that these lines are

not perfectly aligned with the pixel rows in order to prevent artifacts in the spectra if a row is faulty or has a different efficiency. This slight inclination is specified by a slope. Additionally these lines are faintly curved, because of optical aberrations by the spherical grating, the so called coma. The vertical shift of the isoenergetic lines relatively to the pixel row can be described by the following discrete equation:

$$\Delta_j = slope \cdot j + smile \cdot j^2 \tag{3.2}$$

where j is the pixel column index. Then, each column is moved vertically by the quantity $-\Delta_j$ in order to align the lines with the pixel rows: so the spectrum can be obtained by simply summing along the rows of the new matrix. The shift Δ_j should be rounded because the vertical shifts should be integers to define a new pixel matrix, but this determines a maximum error of $\pm$ 0,5 pixel in the shifts, determining a loss in spectral resolution. In the ERIXS spectrometer, the coma can be almost perfectly corrected and the second-order parameter *smile* is not relevant.

Another procedure permits to avoid these rough integers shifts by interpolation between neighbouring pixels. As shown in Figure 3.2, an applied fractional shift to the columns of the old matrix would consist in a new matrix whose cells contain a portion of two neighbouring pixels. The intensity of the new pixel is calculated by interpolation between the pixels of the old matrix where the weights represent the fraction of the old pixel areas lying in the new cell. After interpolation, the spectrum is again obtained by summing along the rows.

In order to improve spectral definition, the channel doubling can be also carried out. If we double the number of cells in each column of the new matrix, after vertical shift each old pixel can overlap up to three cells and the new intensity is again evaluated as a weighted sum according to the

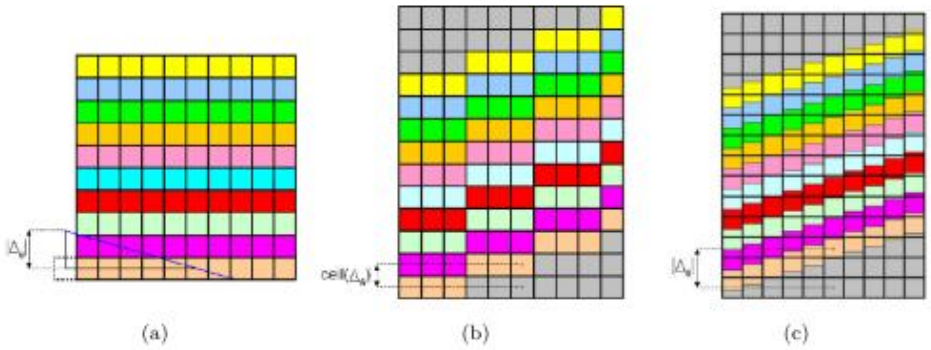

Figure 3.2: Procedure to align the isoenergetic lines with the pixel rows. Colorful rows represent the charges under each pixel, the blue inclined line is the isoenergetic line (a). The column shift applied to the matrix can be an integer number of pixels (b) or the exact fractional value (c).

overlapping percentage. It is important to stress that although doubling the number of experimental points, this procedure does not involve a resolution enhancement because each point is generated by interpolation. The result is only a smoothing of the data that gives a higher definition of the spectrum, because the number of samples is doubled.
This method is very useful and powerful for general applications because, although the obtained resolution is limited by the charge cloud size, it works very well in every working conditions (with no need of low photon flux).

Single Photon Counting algorithm

Single Photon Counting (SPC) technique represents an improvement in term of resolution [12] [19] with respect to the previously described algorithm. Since the charge cloud is shared among several pixels, the idea behind the Single Photon Counting is to try to identify the centre of the intensity distribution which should correspond, within uncertainties, to the photon impact position.
While the Traditional algorithm only uses the total integrated intensity of

many photons events, allowing high photon flux and long exposure time, the SPC involves an image reconstruction, where each photon spot needs to be analysed separately in order to identify the centre of the charge distribution. For this purpose, the spots don't have to overlap and this means that a low photon flux and a short exposure time are required. Then, the final reconstructed image from which the spectrum is calculated, is the sum of several short exposures, in order to have a statistically meaningful signal.
The first step is a background subtraction on the image in a similar way as in the traditional algorithm.
Then, the spot search represents the crucial part of SPC algorithm because it has to recognize all the spots generated by photons of the desired energy and distinguish them from charges of other origin, for example cosmic rays or noise. First of all, according to the energy range of the photons we are interested in, a high and low central pixel threshold (HCPT and LCPT) is required. Although the charge is spread among many pixels, the central one is expected to carry the highest intensity because it is supposed to be the one hit by the photon. Initially, a first search is performed on the entire image in order to identify the ideal candidates to be central pixels of a spot. The spot itself is defined as a N×N pixel matrix centred on each of them. The use of these two threshold doesn't guarantee that only the most intense pixel of a spot is considered. Infact, different situations can happen leading to an unaccurate result. Several procedures have been added to the algorithm in order to overcome possible errors (for a more detailed description see [12]). After recognition, spots are usually separated by intensity using two thresholds: the low and high spot intensity threshold (LSIT and HSIT). These are a further instrument to select photon events with the expected energy. Spots with a lower intensity can be due to strong noisy contributions, whereas spots which are too high in intensity are the result of multiple events and would lead to a wrong centroid reconstruction. Once the N×N spot has been

defined, the calculation of the centroid of the intensity distribution can be performed. Considering that pixel intensities are in some way proportional to their proximity to the photon impact position, the latter can be in first approximation defined as the centre of mass(COM) of the N×N pixel matrix. In terms of image moments the COM is given by:

$$\{x_{COM}, y_{COM}\} = \{\frac{M_{10}}{M_{00}}, \frac{M_{01}}{M_{00}}\} \tag{3.3}$$

where the general moment M_{ij} is deïňĄned as:

$$M_{ij} = \sum_x \sum_y x^i y^j I(x, y) \tag{3.4}$$

in which x, y are the integer pixel coordinates and I is the pixel intensity. In this calculation, considering N×N spots, $-(N-1) < x, y < N-1$ so that for each spot the COM position is specified with respect to its central pixel, which is assigned the location (0, 0) within the spot matrix. The COM coordinate, is then added to the absolute central pixel position in order to relocate the photon hit on the complete image.

The third and last step consists in the elaboration of the spectrum starting from the single photon COM positions, which are defined by a couple of rational numbers (x_{COM}, y_{COM}). In order to get the spectrum, an integration along the isoenergetic lines is again needed, anticipated by a coordinate transformation to make these lines horizontal. This is done by subtracting from the y_{COM} the corresponding shift of the isoenergetic line Δ_y calculated at x_{COM}. The transformation is the following:

$$x'_{COM} = x_{COM} \; y'_{COM} = y_{COM} - \Delta_y \tag{3.5}$$

where $\Delta_j = slope \cdot x_{COM} + smile \cdot x_{COM}^2$. In order to highlight the real resolution enhancement resulting from this method, Figure 3.3 shows a NiO spectrum recently measured with ERIXS in HE configuration, extracted both

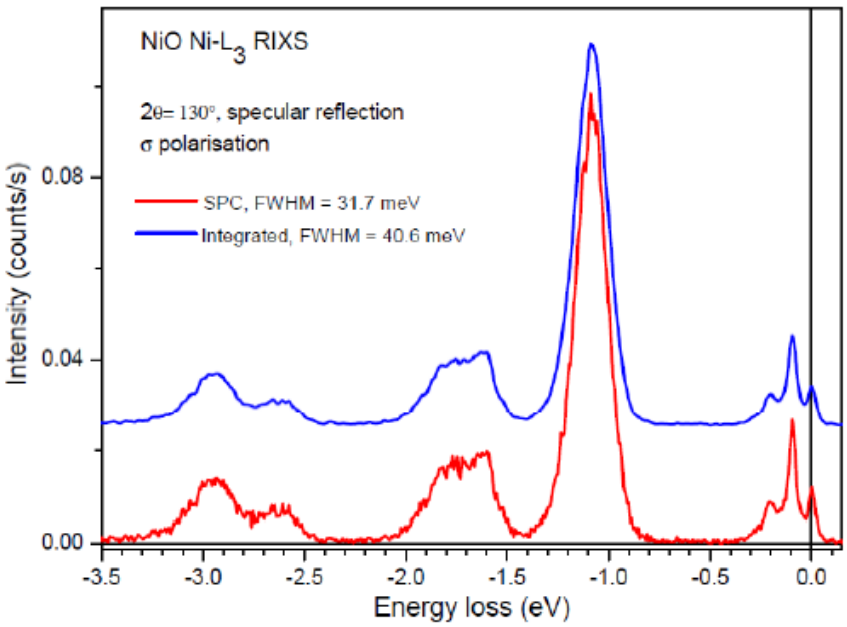

Figure 3.3: NiO, Ni L_3 RIXS spectra recently measured with ERIXS in HE configuration, extracted with traditional integrating algorithm (blue) and SPC (red). Figure reproduced from [23].

with Traditional and Single Photon Counting algorithm. We can see that, compared to NiO spectra in Figure 2.15, the HE configuration allows to distinguish the two magnetic peaks below 500 meV. For a full characterization of the spectrum we refer to Chapter 5, but it is clearly visible that resolution limited peaks (i.e. the elastic and magnetic) get sharper. By comparing the linewidths of these peaks in the two spectra, we can conclude that the SPC algorithm induces an improvement in energy resolution by a factor of $\sim 25\%$ at the Ni-L_3 edge.

After the spectra generation, there are some additional operations to carry out in order to obtain the final energy loss spectrum. First of all, for better statistics, many acquisitions are made in the same conditions. This means that a set of spectra have to be taken into account during the data analysis. In

particular, the total spectrum is generated by summing the individual spectra of this group of images. But, before this, it's important to consider that the acquired images may present some slight variations that correspond to a set of spectra not perfectly aligned. This is due to the fact that the acquisitions are not done simultaneously and the energy of the incoming beam or the position of the detector may drift with time. Therefore, an alignment procedure is performed before the sum. After that, the x-axis of the spectrum is still in pixel indices and needs to be converted in energies. This is done through the energy calibration, which allows this conversion using two parameters: the zero energy pixel and the calibration coefficient. The former, i.e. the zero energy loss position is defined using an elastic peak obtained from a sample that should not exhibit energy losses. A typical material used for this purpose is carbon tape, which is present on the sample holder since it is used to stick the samples on the holder. In order to determine the correspondance pixel↔energy the incoming photon energy is varied leading to a variation of the elastic peaks position on the detector. The plot of the incoming energy versus the peaks positions results in a straight line whose slope is defined as the calibration coefficient between pixels indexes and energy loss. The final energy loss spectrum is finally ready for any further analysis.
The aim of my thesis project was to put all these procedures together in a unique software, written in Python and supported by a user-friendly interface. In the next section a full characterization of my work will be provided.

3.2 RIXSToolbox characterization

The realization of a new data-analysis software for the new ID32 Beamline RIXS end station has been the central topic of my project at the ESRF. It is based on Python, that is a widely used general-purpose, high-level programming language. It is free and has a large standard library, providing

tools suited to many tasks. In addition, Python has a huge number of GUI toolkits available in order to create a useful interface for the users.
The implementation of this software aims to the translation and unification of all the scripts previously used and written in different programming languages making data analysis faster, easier and more intuitive. The main contribution is mainly due to the addition of the interface, which makes the software more user-friendly, with no need for the users to pass by the code itself. An important feature is that it allows to perform all the needed data elaboration, with no need to open any other program. Furthermore, every step has its own window, so basically it is possible to perform every processing with more flexibility. It heavily relies on PyMca, the X-ray fluorescence toolkit developed by the software group of the European Synchrotron Radiation Facility.
The software is organized in the following way: the main interface (shown in Figure 3.4) consists of three primary functionalities which bring to the final results. As already mentioned, these are:

- Generation of spectra from EDF raw images coming from the CCD detector.
- Alignment and sum of the spectra generated in the previous step.
- Energy calibration: conversion from pixels' indexes to energies.

Furthermore, two additional functions allow the calculation of two parameters useful to the above mentioned main functions:

- Calculation of the slope of the isoenergetic lines on the raw image.
- Calculation of the calibration coefficient [meV/px].

In addition, a guide/tutorial is also provided, showing some practical examples of use. As reported in the information box, this software is work in progress and provided "as it is". Any feedback on the software performances

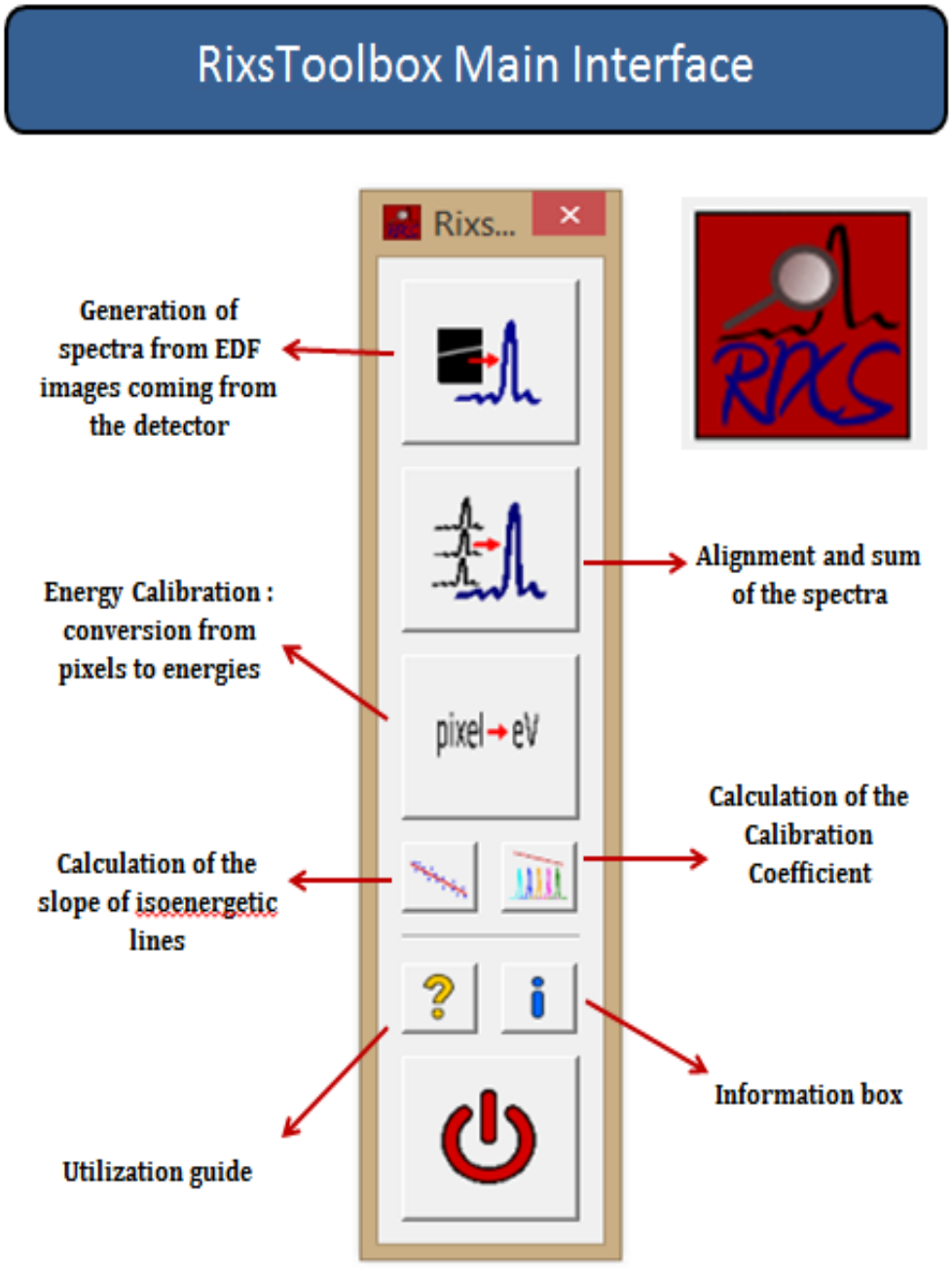

Figure 3.4: Software main interface and brief description of the possible functions.

during its use in experiments by the users will be welcomed and of fundamental importance for a future improvement. The available functionalities are described here, through some schemes illustrating the required inputs and the resulting outputs for the data analysis of a real NiO RIXS spectrum recently measured with ERIXS and that will be discussed in details in Chapter 5. The software interfaces are shown in the Appendix.

Slope Finder

Before starting with the generation of the spectra it's important to calculate the slope of the isoenergetic lines lying on the images to be elaborated. This can be done using several elastic peaks given from a sample that should not exhibit energy losses: carbon tape is a common material used for this purpose. At the end of the process, the corresponding slope values are provided as output. There are two available methods. The first one consists in the spectra extraction using the Traditional algorithm. In particular, one has to select a slope guess, a step and the number of spectra to be generated. As a result, several spectra will be plotted for every input image, varying slope in a range consistent with the chosen parameters. These elastic peaks are analyzed in order to get information about their heights and FWHM, that are plotted and fitted vs slope. These lines show a parabolic trend and their colours help to distinguish between values corresponding to different initial images. In this case, the best slope corresponds to the slope of the spectrum whose peak height is maximum and whose FWHM is minimum. The second method, instead, calculates the slope of the line that fits the central pixels positions that come from the results of the Single Photon Counting algorithm. Figure 3.5 shows a scheme of an example of the graphical and numerical outputs given from the calculation over four carbon tape images. We can see that the results are summarized in a table, together with an average value for every method. Even if they could be not perfectly coincident, the choice

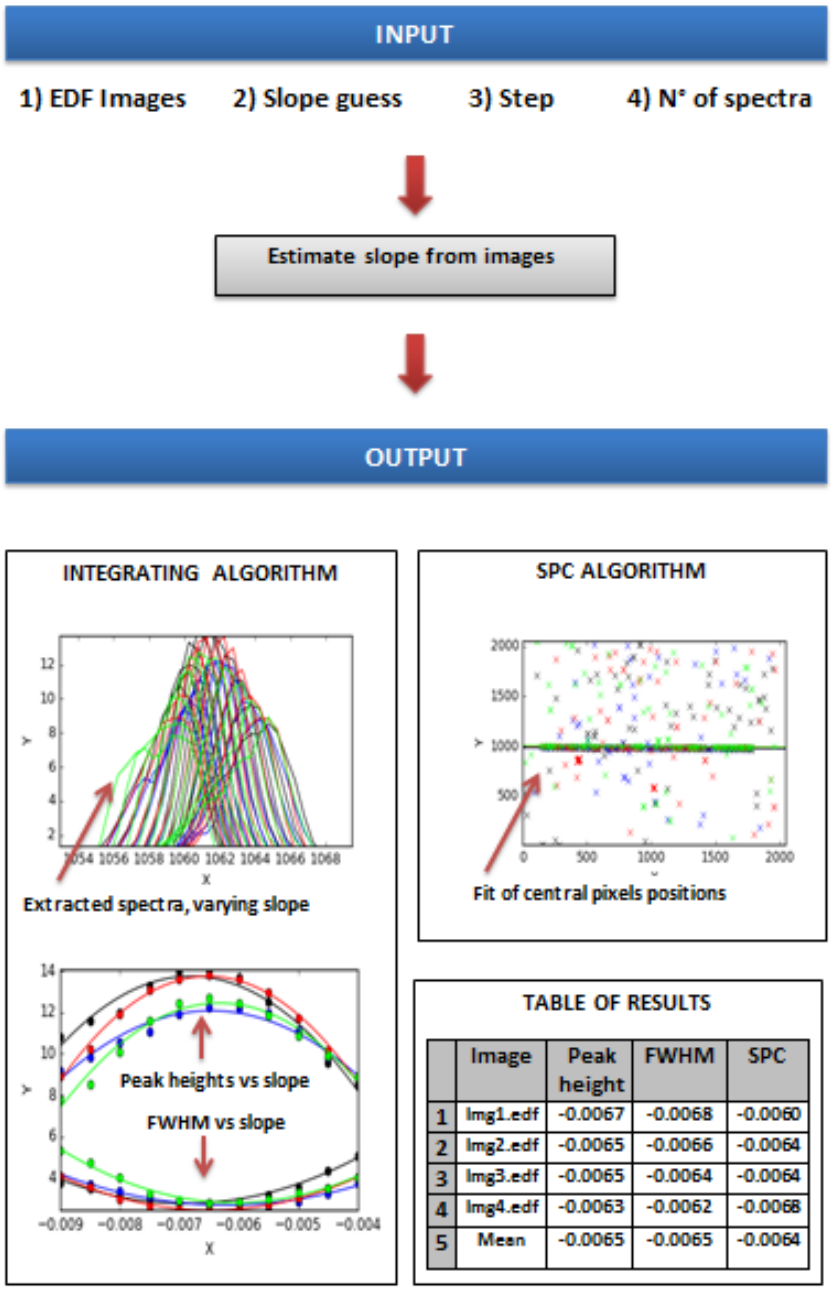

Figure 3.5: Slope Finder functionality: example of the graphical and numerical outputs given from the calculation over 4 carbon tape images.

between them wouldn't affect so much the spectral shape, thus one can use a mean value. Particular attention has been paid to the fit of the central pixels positions. There is a strong presence of outliers that has to be taken into account. In fact, through a standard linear fit minimizing the squared loss, we observed that the outliers exerted a disproportionate influence on the fit. This is due to the nature of the squared loss function, that is overly sensitive to outliers and causes issues with our fit. The solution is to simply adjust the loss function to be more robust. The variety of possible loss functions is quite literally infinite, but one relatively motivated option is the Huber Loss. It defines a critical value at which the loss curve transitions from quadratic to linear, so that the Huber Loss is equivalent to the squared loss for points that are well-fit by the model, but reduces the loss contribution of outliers. A detailed description of the Huber Loss function can be found in [27] together with some practical programming examples [28].

Spectra Generation

Once the slope is calculated, it is possible to insert its value as input in the Spectra Generation window and extract the spectra using the two possible algorithms previously described. The parameters used for these two cases (for example the values of the thresholds) are set by default, but it's also possible to change them. Indeed, the recommended choice of points per pixel to be used for the calculation is 2.7 for a better definition of the spectral shape (this value comes from the need to make the interpolation incommensurate with the pixel period). Once everything is set, one or more images can be selected at the same time and the corresponding spectra will be shown in the plot window, labelled with the name of the EDF image they come from (most data taken with ccd cameras at the ESRF are stored in the EDF, which stands for ESRF Data Format). At the end of the process, the spectra can be saved with the dedicated functionality, after choosing the file name. In

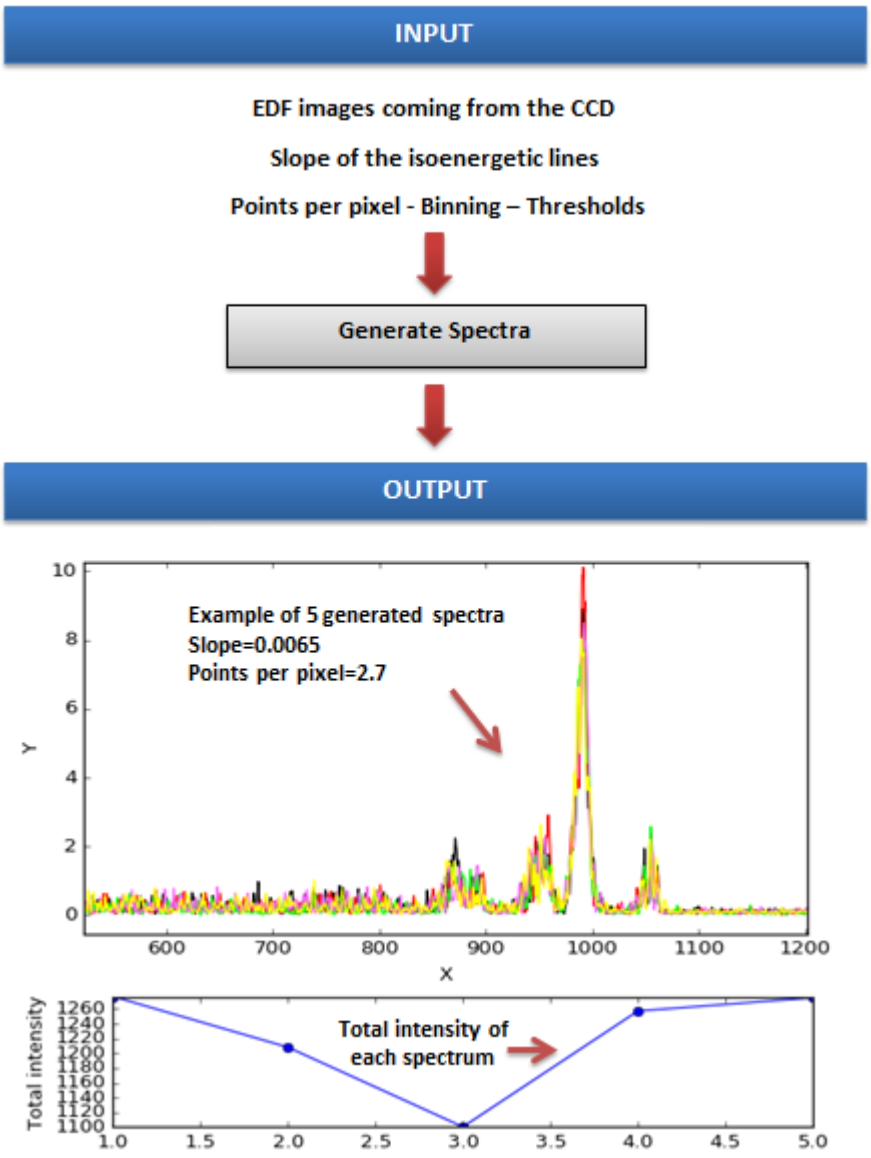

Figure 3.6: Generate Spectra functionality: example of the generation of 5 RIXS spectra.

each saved file from now on, there is an important feature that helps the user understanding what the file refers to. Since it can substantially contain several spectra, it is useful to store information about each of them and this is done in the so called Scan Header of each scan in the file. Figure 3.6 shows a schematic representation of this step. Looking at the most intense feature in the spectra, it is clearly visible that these partial spectra positions show a drift and thus need to be aligned before summing their contributions in order to obtain the total one: this is the purpose of the next step.

Alignment and Sum of the spectra

This functionality permits the alignment of the set of spectra we are analyzing. Typically the first one or the last one can be chosen as reference for the alignment, thus the shifts of the other spectra refer to its position. The alignment is done through a Fast Fourier Transform (FFT) method which calculates the correlation between two curves as a function of the relative shift between them. The relative shift between two shifted but otherwise identical spectra is given by where their correlation function is maximum. The aligned spectra and the corresponding shifts are then plotted and ready for the sum in order to take into account all the contributions coming from the whole set (Figure 3.7). To demonstrate the importance of this step, Figure 3.8 shows three spectra extracted from a set of acquired images. They correspond respectively to the first one, the middle one and the last one of the set. We can see that they are not perfectly aligned and this will have an impact to the sum. In fact, the summed spectrum obtained after the alignment is better resolved and much closer to the result we are looking for. After this step, what is missing is the information about the energy loss characteristic of every peak. In fact, we can notice that the x-axis of the plot is still in pixel indices, so we need to convert pixels to energies using a particular conversion coefficient: this step is called energy calibration.

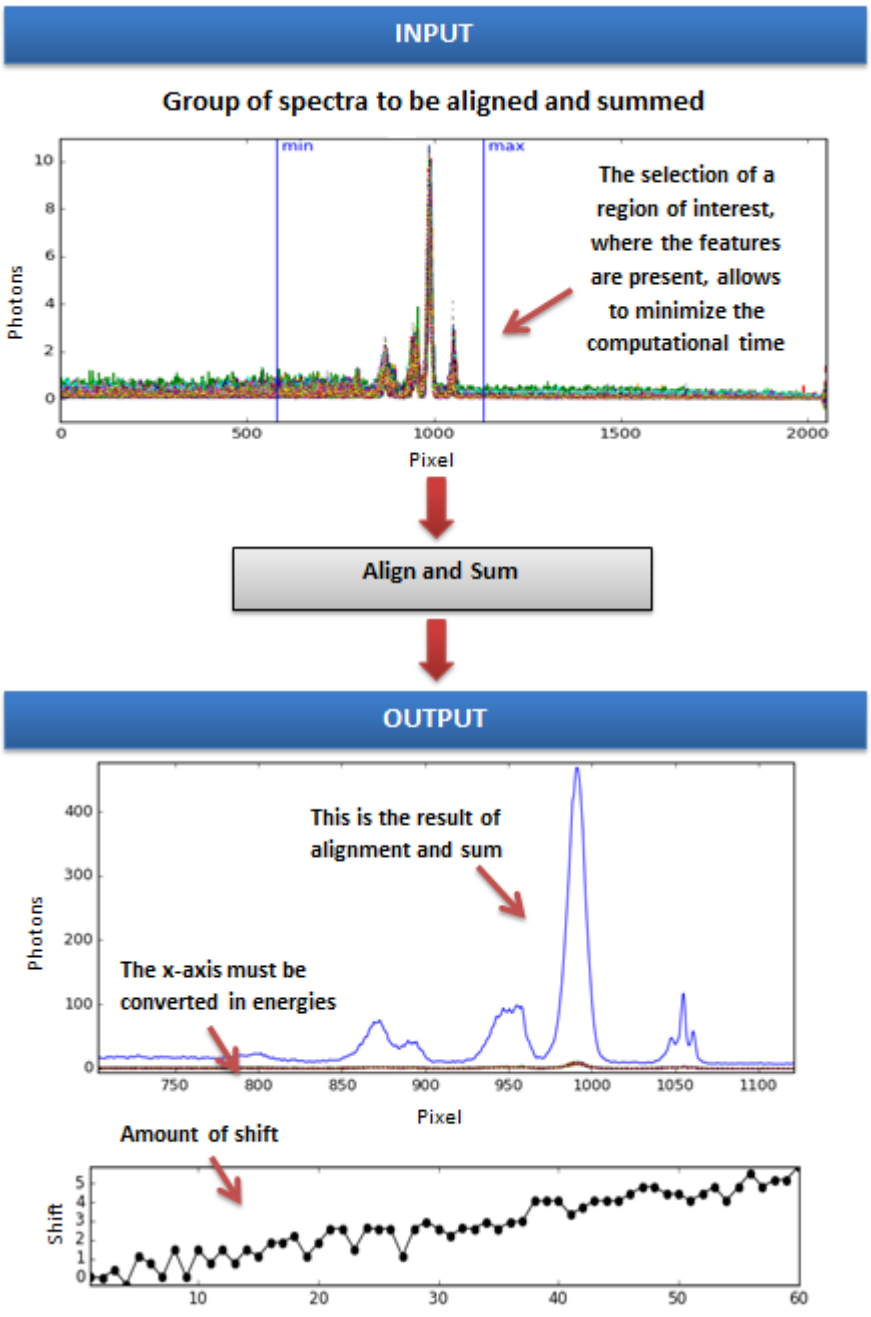

Figure 3.7: Alignment and Sum: the set of generated spectra needs to be aligned and then summed in order to obtain the total spectrum.

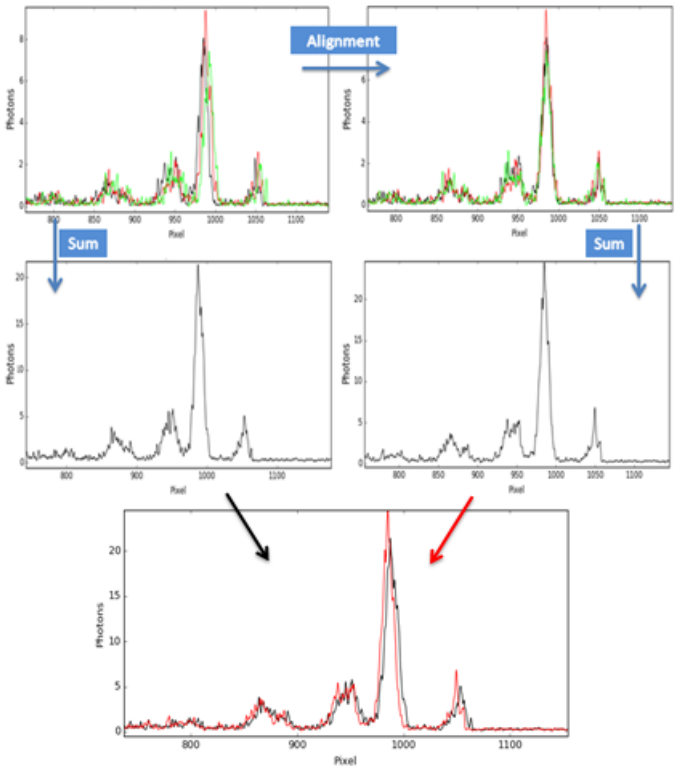

Figure 3.8: Comparison between summed spectra with (red) and without (black) alignment.

Calibration coefficient calculation

As already explained, the calibration coefficient is useful for the energy calibration step. It is quickly calculated loading several carbon tape scans taken with varying incident energy. As a result, the positions of the elastic peaks are slightly different and this is also shown in the plot window of the interface. Then, we need two information coming from these spectra: their incident energy and their relative shifts. The former is automatically obtained because this information is stored in the scan header of the file. The latter can be fast computed performing an alignment of every spectrum taking the first one as reference and recording the amount of shift of each one. After plotting these shifts vs the corresponding incident energy and performing

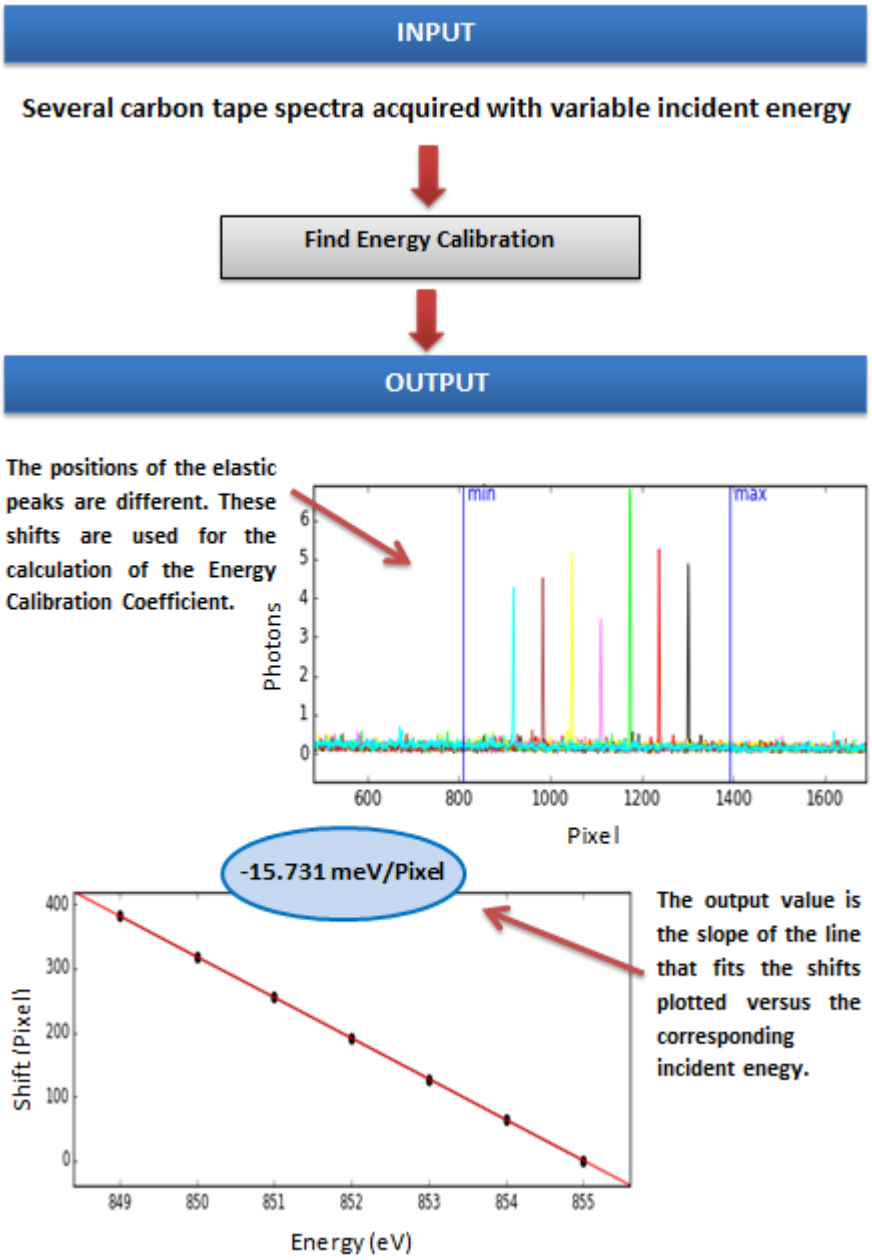

Figure 3.9: Energy Calibration Calculation functionality: example of the graphical and numerical outputs.

a linear fit, the slope of this line gives the value of the coefficient we are interested in. Figure 3.9 summarizes this step.

Energy Calibration

The Energy Calibration is the final step of the procedure, consisting in conversion from pixels to energies in order to obtain an energy loss spectrum. Two parameters need to be set: the Calibration coefficient [meV/pixel] and the Zero energy pixel. The first one has just been explained. The second one is defined as the position of the elastic peak given from a carbon tape sample that was acquired just after or before the spectrum that was chosen as the reference for the alignment. Once these values are determined, one can simply load the spectrum to be calibrated and start the conversion. The final energy loss spectrum is then plotted (as shown in Figure 3.10) and all the information about the calibration are stored in the Scan Header of the file once is saved.

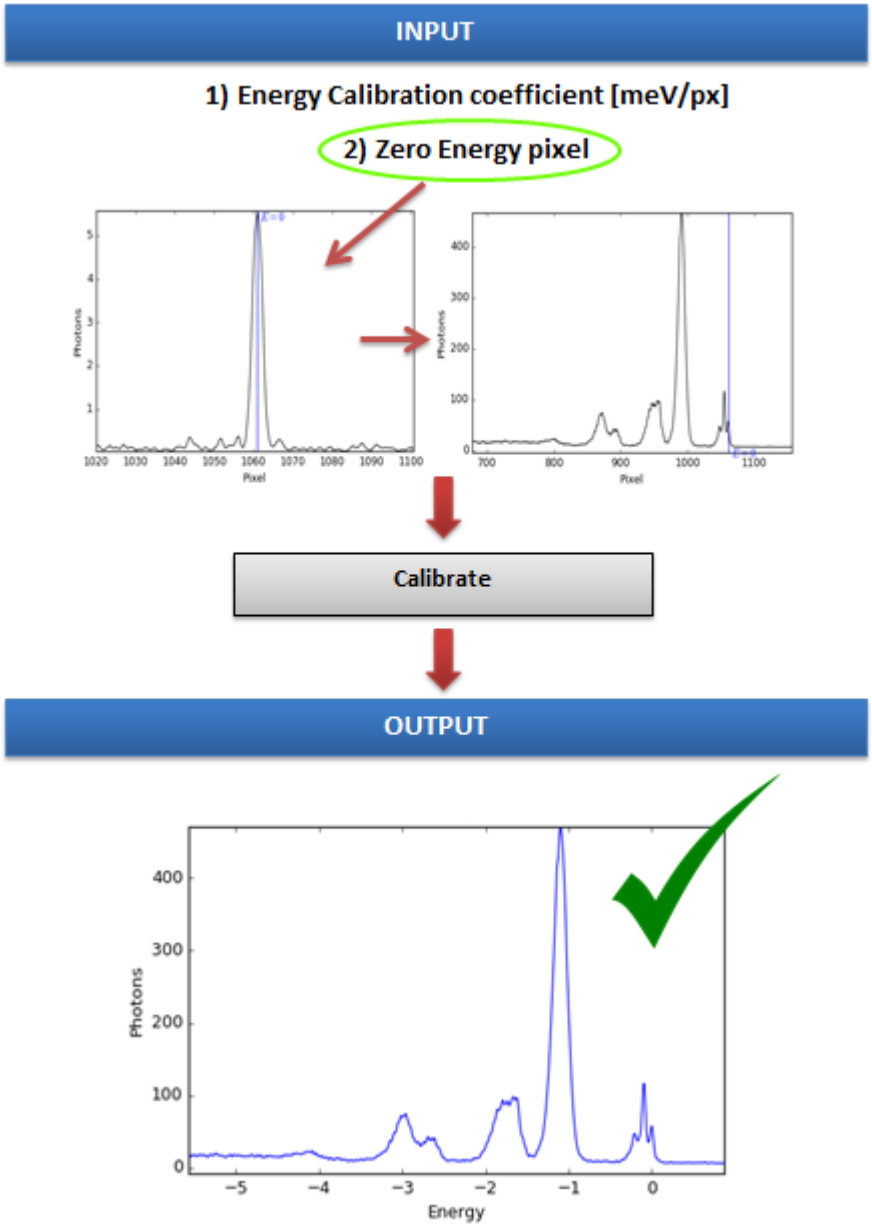

Figure 3.10: Application of the energy calibration: the output is the final energy loss spectrum.

4

NiO as a case of interest for high resolution RIXS

This Chapter, together with Chapter 5, aims to highlight the versatility and potentialities of RIXS spectroscopy, showing the evolution of the experimental results collected during the last decade. We particularly focus on the use of RIXS on the class of strongly correlated electron systems. They have received a great deal of attention over the years, because of their unexpected physical properties, such as high-T_C superconductivity and colossal magnetoresistance, that could lead to possible technological applications. However, these systems are still far from being fully understood. Exploiting RIXS with its modern available instrumentation could help to significantly improve our understanding of their peculiar properties and the underlying physics. Here, we present an example of a strongly correlated system, NiO, which has a $3d^8$ configuration. Although simple band theory predicts it to be a good conductor, it is an antiferromagnetic insulator at room temperature with a relatively large band gap, which is determined to be about 4 eV by optical measurements. Soft X-rays RIXS is a suitable technique for the investigation of this type of material, since the K edge of O and the $L_{2,3}$ edges of $3d$ transition-metal compounds lie in the soft X-ray range. In particular, NiO has received a lot of interest in the last years because the instrumentation

improvements led to significant results in terms of resolution. Thus, we can use NiO as a test for high resolution RIXS, in order to show the nowadays available performances, as we will see in Chapter 5.

4.1 Strongly correlated electron systems

NiO, one of the most favored antiferromagnets, belongs to the class of $3d$ transition-metal oxides (TMOs) and is classified as a strongly correlated electron system. These materials are characterized by a strong interaction between their electrons and cannot be described by models based on single electron approach. In fact, the so called mean field theories, which consider an electron propagating in a periodic field generating by the atoms nuclei and an average Coulomb field due to the presence of other electrons in the solid, are no longer valid for these compounds. This is because each single electron has a complex influence on its neighbors. Indeed, one-electron theory predicts metallic behavior for many $3d$ transition-metal oxides, but they actually are insulators with large band gaps. For instance, NiO has a partially filled $3d$ band (the Ni atom has 8 of 10 possible $3d$-electrons) and therefore would be expected to be a good conductor. However, strong Coulomb repulsion between d-electrons makes NiO a wide band gap insulator.
In order to properly reconcile the complexity of strongly correlated systems, it is necessary to introduce many-body calculations. On the other hand, such calculations are very difficult to handle because of the large number of electrons involved. Thus, model Hamiltonians should be developed in order to properly describe the essential phenomena but neglecting some interactions between electrons. One of the simplest model Hamiltonians was proposed by Hubbard in 1963 [29], which is a development of the tight-binding model. The Hubbard Hamiltonian is mainly described by two terms that are competing, one relative to the Coulomb interaction U and the other one is

the kinetic term, described by the hopping integral t between adjacent sites as in the tight-binding Hamiltonian. The hopping integral is proportional to the bandwidth W and is referable to how the electrons move in a conductor, while the Coulomb interaction forces the electrons to stay localized in their sites. The Hubbard Hamiltonian is:

$$\mathcal{H} = \sum_{i,j} \sum_{\sigma} t_{ij} (\mathbf{c}^{\dagger}_{i\sigma} \mathbf{c}_{j\sigma} + \mathbf{c}^{\dagger}_{j\sigma} \mathbf{c}_{i\sigma}) + U \sum_{i} \mathbf{n}_{i\uparrow} \mathbf{n}_{i\downarrow} \tag{4.1}$$

where t_{ij} is the hopping integral, $\mathbf{c}^{\dagger}_{i\sigma}(\mathbf{c}_{i\sigma})$ are the creation (annihilation) operators of electrons with spin σ and $\mathbf{n}_{i\sigma} = \mathbf{c}^{\dagger}_{i\sigma}\mathbf{c}_{i\sigma}$ is the number operator. The physics of the system is dictated by the relative strength of electron localisation (U) and delocalisation (t). In fact, if U/t$\rightarrow$0 the system is metallic, while if U/t$\rightarrow \infty$ the system is an insulator because the double occupation of the same site is energetically unfavourable. The transition between these two regimes is the so-called "Mott-Hubbard" transition. In Figure 4.1 we can see the evolution of the density of states of a model material as a function of U/t (or U/W). For U=0 the Fermi level is located in the middle of the valence band. Larger values of U affect the shape of the density of states by moving states away from the Fermi level. In the large U limit, we can distinguish two bands, one entirely filled below the Fermi energy and one entirely empty above; these are usually called the lower Hubbard and the higher Hubbard bands, respectively. Their energy separation, the band gap scales with U.
After this brief description of these systems, we introduce the case of NiO, presenting the main properties which allow to understand the spectral features in the RIXS spectrum that will be shown in Chapter 5.

4.2 NiO atomic structure

NiO is antiferromagnetic at room temperature and has a rock-salt cubic structure, where Ni ions occupy octahedral sites, with a lattice constant of

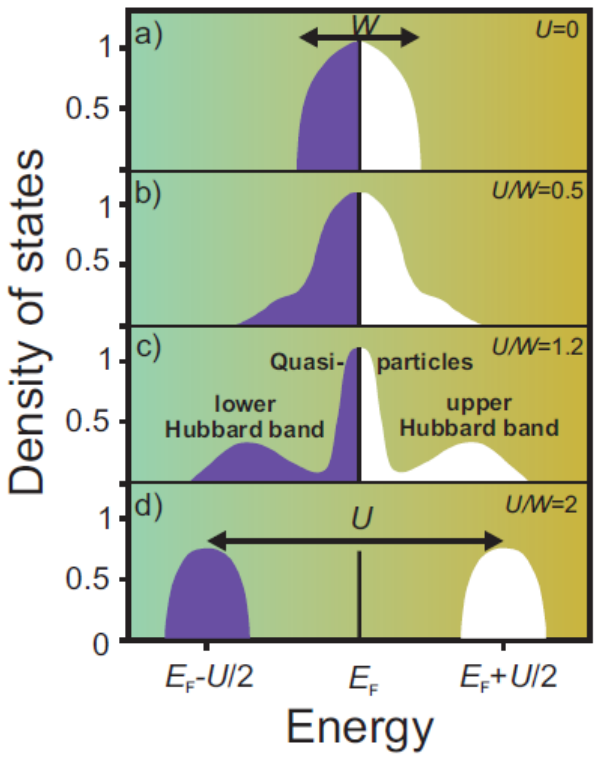

Figure 4.1: The density of states (DOS) of electrons in a dynamical mean-field solution of the Hubbard model where U is the Coulomb interaction energy and W the bandwidth of non-interacting electrons which is proportional to the hopping integral. (a) For $U = 0$ (metallic case), the Fermi level lies in the middle of the band. In the weakly correlated regime (small U/W) electrons can be classified as quasiparticle whose DOS resembles the one of free electrons. If $U/W > 1$ the correlation increases and the spectrum (c) shows three peaks that are typical in correlated metals. Finally (d), in the strongly correlated regime ($U/W \gg 1$) a Mott-Hubbard transition to an insulating state takes place. Figure taken from [29].

a=4.17 Å (see Figure 4.2). There are two components of spin configurations due to the non-local exchange interaction [30]. For the first component, the direct exchange interaction between the nearest neighbour of Ni ions favors pairing of spins to lower energy. For the second one, a very strong interaction comes from the superexchange between the next-nearest neighbour of Ni ions. This is responsible for the antiferromagnetic spin structure in the ground state of NiO with a Neel temperature T_N=523 K. Figure 4.3

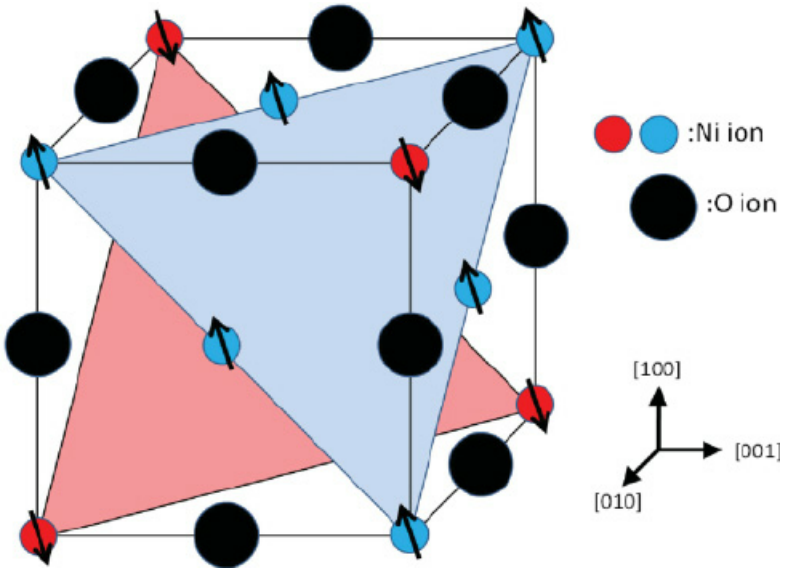

Figure 4.2: Schematic illustration of the spin structure in NiO. Taken from [31].

shows a schematic representation of the atomic model with configuration interaction used to describe the electronic structure of NiO in the ground and excited states. This picture is useful to understand the RIXS process depicted in the lower part of the figure. The ground state is characterized by having n=8 electrons in the $3d$ orbitals while the intermediate one has n+1=9 electrons (n represents the $3d$ orbital occupancy). The covalency of the Ni-O bond is taken into account by two atomic configuration, having n and n+1 $3d$ occupancy at the Ni sites. The two non-interacting configurations ($3d^n$ and $3d^{n+1}\underline{L}$) of the ground state are split by the so-called charge transfer

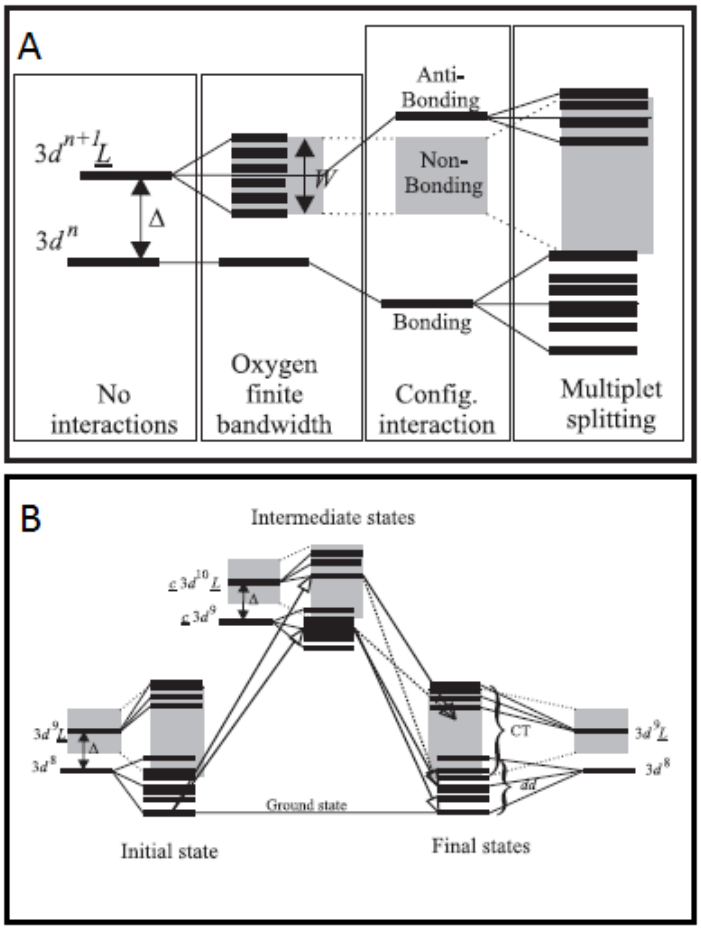

Figure 4.3: Upper panel: Representation of the atomic model with configuration interaction used to describe the electronic structure of NiO in the ground and excited states. Lower panel: Scheme of the L_3 RIXS process. Taken from [11].

energy (CT), indicated by Δ. In our treatment, charge transfer excitations are labelled by $3d^{n+1}\underline{L}$, where $\underline{L}$ indicates a ligand hole. Regarding this last configuration, it is characterized by a finite bandwidth W due to the delocalized character of $2p$ states. Moreover, if we take into account the overlap between the two configurations (which depends on the hybridization of Ni $3d$ and O $2p$ states), we obtain three different configurations: two of mixed character (bonding and anti-bonding) spaced by a quantity bigger than Δ, and another one (non-bonding) whose energy is basically not altered by the

hybridization. The bonding and anti-bonding states still have $3d^n$ and $3d^{n+1}$ character and a localized nature, while the non-bonding states (which have also $3d^{n+1}$ character and are charge transfer states) are delocalized and form a continuum. Considering that in NiO the anti-bonding and non-bonding states are probably indistinguishable [32], we will consider the charge transfer states as an ensemble of states distribuited over a quasi-continuous range. Finally, in order to better describe the electronic structure of NiO we have to consider the effect of intra Coulomb interaction and the effect of the crystal field, which splits the two configurations in multiplets.

After these consideration, we can introduce what types of information RIXS can give us. RIXS is a second order process, and in case of NiO the double radiative transition can be written in the following schematic way: $3d^n \rightarrow 2p^5 3d^{n+1} \rightarrow [3d^n;\ 3d^{n*};\ 3d^{n+1}\underline{L}]$. Here $3d^{n*}$ represents a final state in the RIXS process different from the initial one: the final state has the same number of electrons in $3d$ orbitals, but at the end of the process we can have a redistribution of the electrons among the available orbitals (the so called *dd* excitations).

In Figure 4.3 a representation of the L_3 RIXS process is shown, illustrating the possible transitions. The system is initially in its ground state. Upon absorption of one X-ray photon, the system reaches its intermediate state, which is determined by the energy and polarization of the incident photon. Then, a photon of given polarization and energy is emitted, leading to one of the possible final states. For instance, if the intermediate state has mainly $3d^9$ ($3d^{10}\underline{L}$) character, the final state will more likely be of *dd* (charge transfer) type. Since *dd* excitations and CT are well separated in energy in this case, it is possible to enhance one of the two by properly tuning the incident photon energy.

5 Experimental results at Ni L_3-edge

I show here the most remarkable results obtained with RIXS for NiO in the last years, together with a recent measurement using the ERIXS spectrometer, at ID32 Beamline of the ESRF and the RixsToolBox software developed as part of this project. The great potential of this new instrumentation is highlighted by the visible progress on the spectrum definition, allowing to resolve some spectral features that otherwise would not be seen. This enhancement marks a major step in the study of such complex systems, because it can resolve the relevant excitations and thus provide more information useful for a better characterization.

5.1 Experimental progress of the last decade

I present now some experimental results achieved during the last decade, showing how RIXS has been exploited leading to a considerable progress. We start from a measurement carried out at the old Beamline ID08 at ESRF, using the AXES spectrometer, by the group of G. Ghiringhelli, L. Braicovich and N. Brookes in 2005 [11]. The experimental geometry is sketched in the upper part of Figure 5.1. The scattering angle was 110° in the horizontal plane. The incident beam was impinging at 20° from the (001) surface and

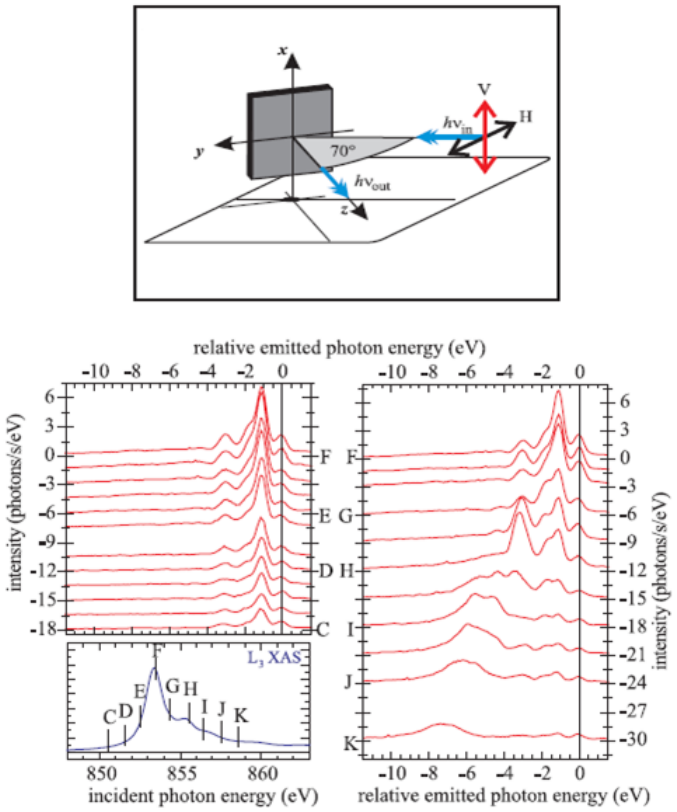

Figure 5.1: Experimental NiO L_3 RIXS spectra measured with AXES. The lower panel shows the XAS spectrum and the labels of the excitations energies used for the RIXS spectra. The polarization of the incident energy was V-pol. Reproduced from [11].

the analysed radiation was along the [001] direction, normal to the sample surface. The polarization of the incident radiation was set either lying in the scattering plane (H-pol for horizontal polarization) or perpendicular to the scattering plane (V-pol for vertical polarization). The lower part of Figure 5.1 shows one set of RIXS spectra taken across the Ni L_3 edge with a measured combined resolution of 750 meV and V-pol. The labels indicate the excitation energies, that correspond to the ones in the absorption spectrum (e.g. F for the L_3 peak). We can see the evolution of the spectra as a result of a variable incident energy. In particular, below the point F + 0.5 eV, i.e. in the left part

of the figure, the spectral shape evolves very little and we recognize the elastic peak, a main peak around 1.1 eV, one shoulder at 1.8 eV, one peak at 3.0 eV and a long tail below 4 eV. Above the main peak, the spectra change shape at every excitation energy, but the position of the peaks is almost constant between 4 eV and 0. Indeed, we can recognize another peak at 4.2 eV in the spectra from G to I. From excitation H to K the low energy tail is increasingly more intense and disperses towards lower energies: this behaviour is typical of X-ray fluorescence emission, but we are interested in the pure Raman part of the spectra. These results demonstrate that is possible to enhance one region of the spectra, depending on which we are interested in. Moreover, the shown data are consistent with those previously measured by Ishii et al [33] and by Magnuson et al [34], but the better energy resolution and statistical quality allowed to unravel a more detailed spectral structure.

Despite this great improvement, practical limitations couldn't allow to demonstrate empirically the prediction of De Groot, Kuiper and Sawatzky [35] who pointed out the possibility of measuring local spin-flip excitations by RIXS performed at the $L_{2,3}$ ($2p \rightarrow 3d$) and $M_{2,3}$ ($3p \rightarrow 3d$) absorption edges of transition metal compounds. In fact, the insufficient energy resolution at the L edges and unfavorable inelastic to elastic intensity ratio at the M edges, have inhibited the observation of excitations below 500 meV. Few years later, important technical advances opened new opportunities for RIXS both for hard [36] and soft X-rays [37]: collective magnetic excitations have been observed in cuprates at the Cu K ($1s \rightarrow 4p$) [38] and L_3 edges [8]. I show now the further improvement obtained with SAXES at the ADDRESS Beamline at SLS by Ghiringhelli *et al.* in 2009 [21]. Figure 5.2 shows Ni L_3 RIXS spectra measured on NiO, at 90° scattering angle. In the top panel there is the XAS spectrum with arrows indicating the main peak (P) and main satellite (S) excitations energy selected for the acquisition. In the lower part, the RIXS intensity across the L_3 edge is shown as a colormap which combines RIXS

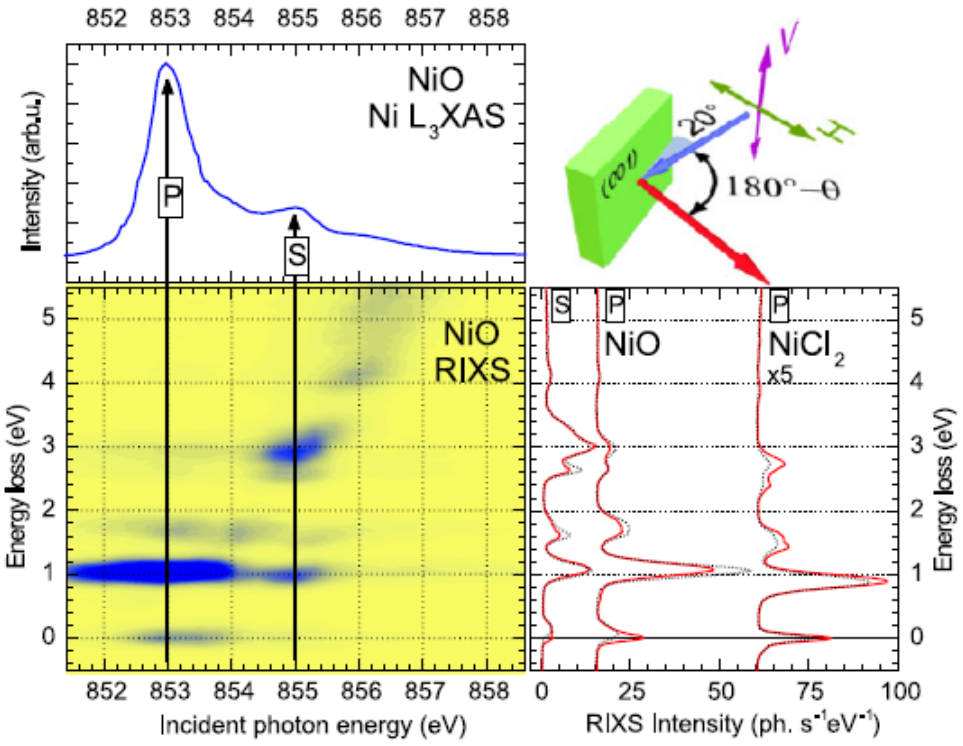

Figure 5.2: Experimental NiO L_3 RIXS spectra measured with SAXES. Reproduced from [21].

spectra measured every 200 meV. The right panel contains the scattering geometry (upper part) and the RIXS spectra (lower part) of NiO and $NiCl_2$ acquired with incident energy corresponding to P and S peaks of the XAS with V-pol (red) and H-pol (black). The measurement temperature T=300 K was below the Néel temperature of NiO, but well above that of $NiCl_2$ (52.3 K). The spectra were in good agreement with literature, but all spectral features are much better defined, due to the further gain in resolution. A remarkable though small difference was found close to the (quasi) elastic peak. While in $NiCl_2$ the line shape is always Gaussian, in NiO we see a broader and asymmetrical line, due to the features between 80-100 meV. In fact, the two sample mainly differ in the size of the superexchange interaction, 10 times

higher in the oxide than in chloride, thus magnetic excitations in $NiCl_2$ are incorporated in the elastic peak whereas they can be detectable in NiO, thanks to the available resolution. In particular, two peaks dominate the spectra, the second at twice the energy of the first one and it was experimentally shown that their relative intensities change with excitation energy and photon polarization but not much with the scattering angle. They can be referred to as atomic spin-flip (ASF) excitations, which have local character. The data presented here demonstrate that also magnetic excitations can be well observed by RIXS and surely a further gain in resolution would lead to a better insight on the dispersion properties of magnetic excitations in AFM compounds. That will be made possible through the new high resolution spectrometer ERIXS at ID32 Beamline at ESRF in Grenoble, which boasts an unprecedent energy resolution. It is open to the users since few months and the early results look promising.

5.2 Recently measured NiO RIXS spectrum with ERIXS

I show now, in Figure 5.3 , a recently measured NiO spectrum, which confirms the reached goals. The excitation energy was 851.11 eV, corresponding to the Ni-L_3 edge in the XAS spectrum (upper part of the figure). The scattering geometry is characterized by 2θ=130°, specular reflection and V-pol. The spectrum is extracted with both Traditional (green) and SPC (red) algorithm. The experiment has been carried out in HE configuration, making possible to clearly distinguish the two magnetic peaks below 500 meV. Moreover, moving from traditional to SPC, we clearly see how the resolution limited peaks get sharper, i.e. the elastic and magnetic peaks, while the *dd* excitations width is limited by intrinsic broadening. In fact, the introduction of SPC provides an improvement by a factor of $\sim 25\%$ at

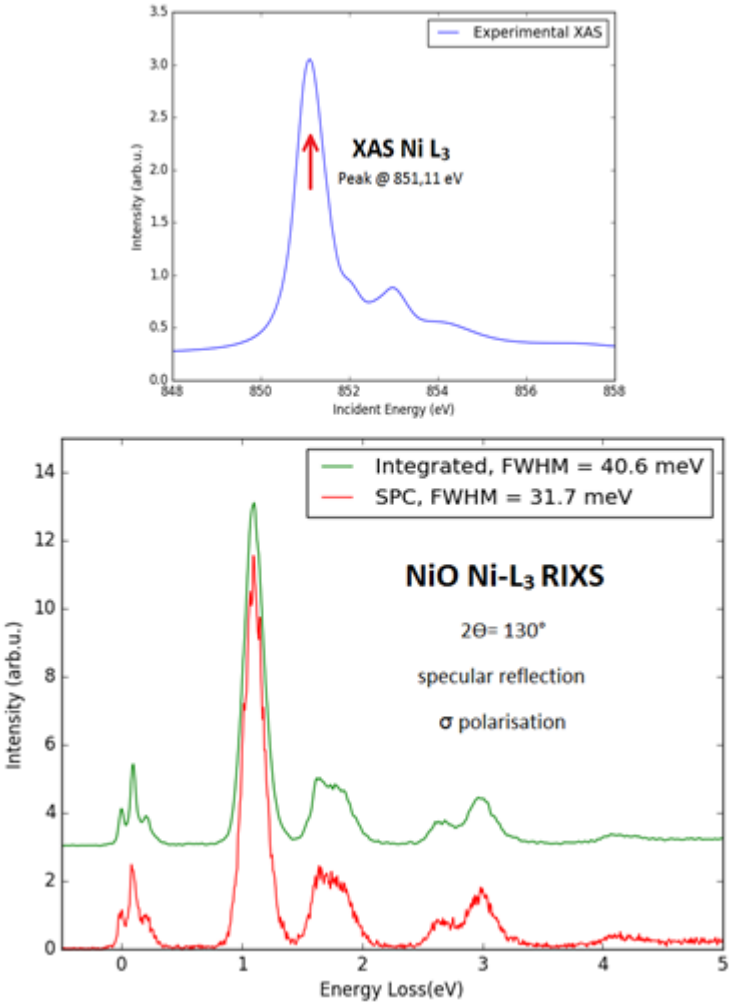

Figure 5.3: Experimental NiO L_3 RIXS spectrum recently measured with ERIXS in HE configuration at the new ID32 Beamline at ESRF. The spectrum is extracted both with Traditional and SPC algorithm, showing an enhancement in resolution by a factor of $\sim 25\%$ at the Ni-L_3 edge. It clearly shows rich dd excitations and double magnetic peak, thanks to the improvement in instrumentation.

the Ni-L_3 edge in terms of energy resolution. Indeed, this spectrum is in agreement with calculations simulating the *dd* excitations in NiO based on a crystal field model. I simulated the process $2p^6 3d^8 \rightarrow 2p^5 3d^9 \rightarrow 2p^6 3d^8$, including crystal field and exchange interaction, using the Quanty code by M.W.Haverkort. Crystal field theory (CFT) is a model that describes the breaking of degeneracies of electronic orbital states, usually *d* or *f*-orbitals, due to a static electric field produced by a surrounding charge distribution. It is developed by considering the energy changes of the five degenerate *d*-orbitals upon being surrounded by an array of point charges, i.e. the ligands. As a ligand approaches the metal ion, the electrons from the ligand will be closer to some of the d-orbitals and farther away from others causing a loss of degeneracy. The electrons in the *d*-orbitals and those in the ligand repel each other due to repulsion between like charges. Thus, the *d*-electrons closer to the ligands will have a higher energy than those further away which results in the *d*-orbitals splitting in energy. In octahedral symmetry (that is the case of NiO), the crystal field split a $3d$ configuration into an e_g and a t_{2g} configuration. t_{2g} consists of the d_{xy}, d_{xz} and d_{yz} orbitals which will be lower in energy than the e_g configuration, consisting of the higher energy d_{z^2} and $d_{x^2-y^2}$ orbitals. The t_{2g} group is lower in energy because it is farther from the ligands than the e_g group and therefore experiences less repulsion. The distance between these two groups is taken into account by the parameter 10Dq. Then, in order to consider the hybridization with the neighbouring atoms, the normal practice is to reduce the Slater integrals. Figure 5.4 shows the result of the calculations compared with the experimental spectrum. The 10Dq and the Slater integrals act on different part of the spectrum: in our case, the first peak at 1.05 eV determines the optimum 10Dq=1.05 and the peak at 3 eV fixes the Slater integral to 65% of their atomic value. The charge transfer excitations are absent as the only possible final states included in the calculations have a $3d^8$ configuration. The parameters used were: 10Dq=1.05,

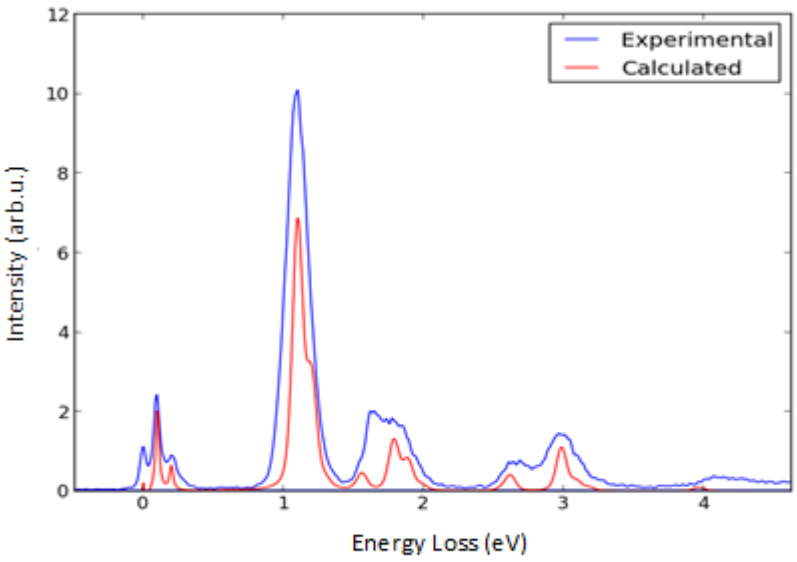

Figure 5.4: Comparison between NiO L_3 RIXS experimental and simulated spectrum. Parameters: 10Dq=1.05, Slater reduction=0.65, exchange force=120 meV, intermediate state lifetime broadening=800 meV, final state lifetime broadening=30 meV. The features above 0.5 eV are convoluted with a Gaussian 400 meV FWHM to simulate their intrinsic broadening.

Slater reduction=0.65, exchange force=120 meV, intermediate state life time broadening=800 meV, final state lifetime= 30 meV. The elastic peak was subtracted, to better distinguish the magnetic excitations. The features above 0.5 eV were then convoluted with a Gaussian 400 meV FWHM to simulate the intrinsic broadening that limits their width. The two spectra look very similar, except for few peaks that are missing and require a more detailed study, but this goes beyond the purpose of this thesis.

To summarize, I showed here how the enhancement became possible through the last decade, using NiO as an example in this case. Obviously there are several systems currently under study through RIXS spectroscopy and this demonstrates the versatility and the great potentialities of this technique. To conclude, after all these considerations, I can say that the contributions

coming from the innovation in the instrumentation and the implementation of dedicated algorithms become the notable key to better understand the physics behind the materials under study.

6 Summary

RIXS in the soft X-ray range is a powerful tool for studying electronic and magnetic excitations in strongly correlated systems. With the new ERIXS spectrometer at the ID32 Beamline of the ESRF another milestone for this experimental technique has been reached. In this thesis I discussed the capabilities of RIXS to characterise strongly correlated systems and described the main features of the ID32 Beamline and the new ERIXS spectrometer up to the detector. In order to make efficient use of this instrument, easy-to-use data analysis is required to help converting the detector images into high-statistics RIXS spectra without compromising the energy resolution. Such software including a graphical user interface has been implemented in the framework of this thesis and is now in routine use at the Beamline. The main features of the software are described in this thesis. The benefits of the new spectrometer and the data analysis software are shown at the example of NiO oxide where the collective magnetic excitations lying below 500 meV were fully resolved for the first time with soft X-ray RIXS. The NiO data is discussed and compared with multiplet calculations including crystal field and exchange interactions.

Appendix

The interfaces of the RIXSToolbox software are shown here. There are five independent windows, one for each functionality: Generation of the spectra, Alignment and Sum, Energy Calibration, Slope Finder, Calculation of the coefficient for the calibration.

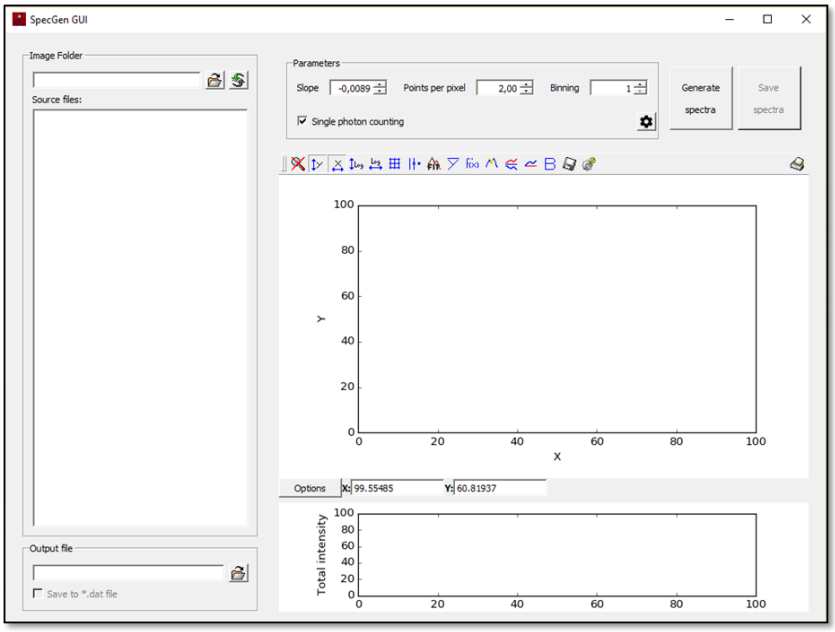

Figure 1: Generate Spectra Interface.

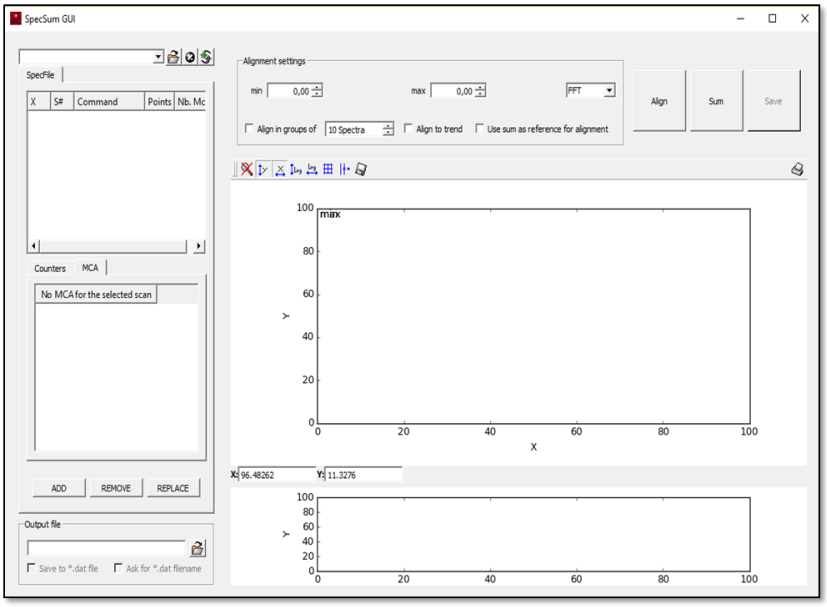

Figure 2: Sum Spectra Interface.

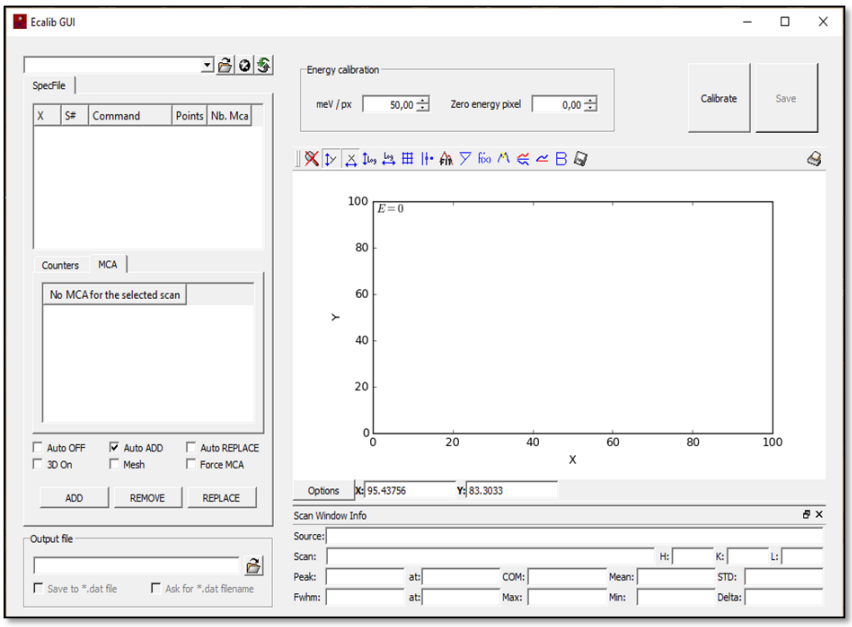

Figure 3: Energy Calibration Interface.

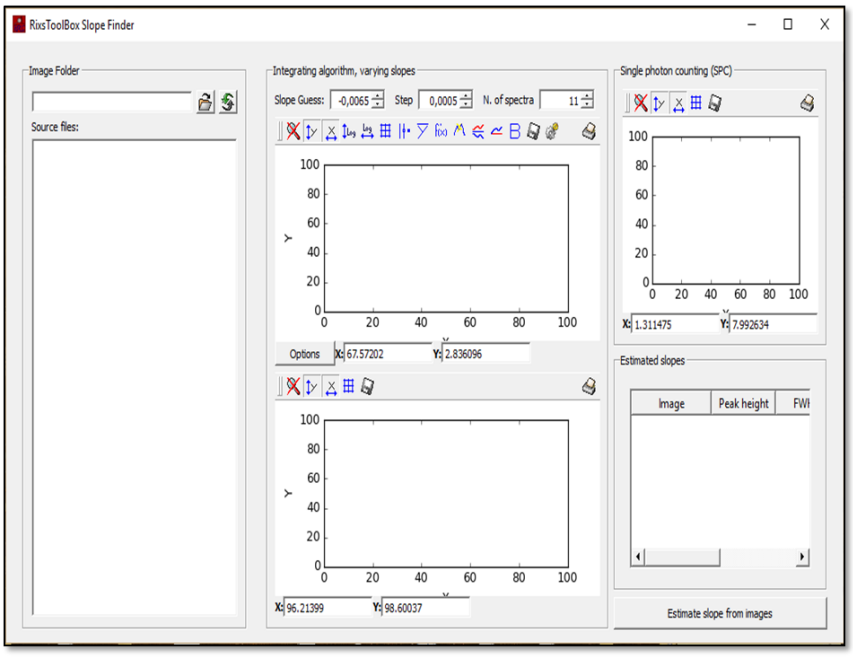

Figure 4: Slope Finder Interface.

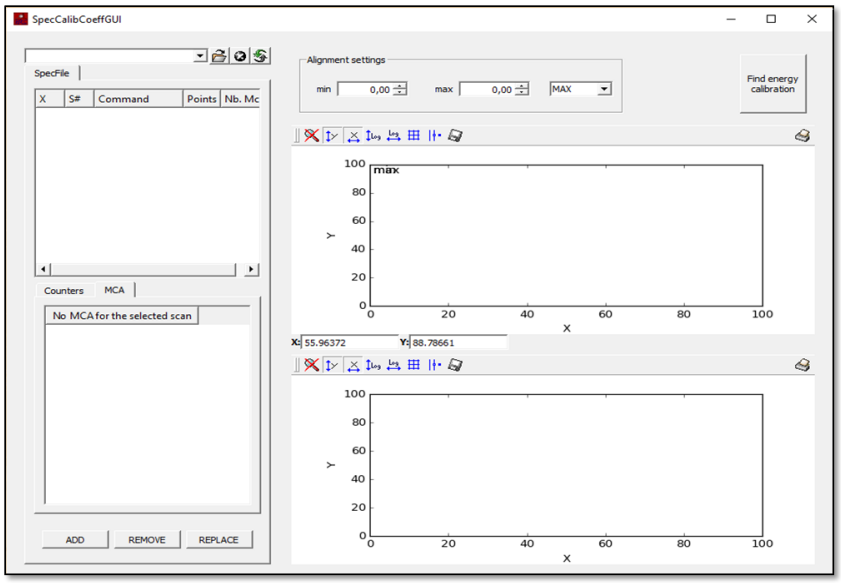

Figure 5: Calibration Coefficient Interface.

Acknowledgments

There are several people that I want to express my gratitude to.
First of all, to my professor Giacomo Ghiringhelli, who gave me the opportunity to live this great experience that taught me a lot from every point of view.
Thanks to Dr. Nick Brookes, for hosting me at the ID32 Beamline for six months.
Thanks to the ID32 staff. To Flora, the strongest woman that I've ever met, always full of energy and positivity.
To Andrea F., my reference point since the beginning.
To Emilio, Davide and Marianne for the nice nights spent together and for making me feel at home.
To Andrea A. for his helpful explanations and suggestions.
But in particular, I want to thank Kurt, I couldn't have had a better supervisor than him, I'm grateful for what he has taught me and for his encouraging words that have been very useful to reach all of my goals.
I also want to thank all of the people that I met in Grenoble, expecially Diletta for her precious support.
Thanks to my favourite girls: Elisa, Pamela, Roberta and Vita, for their

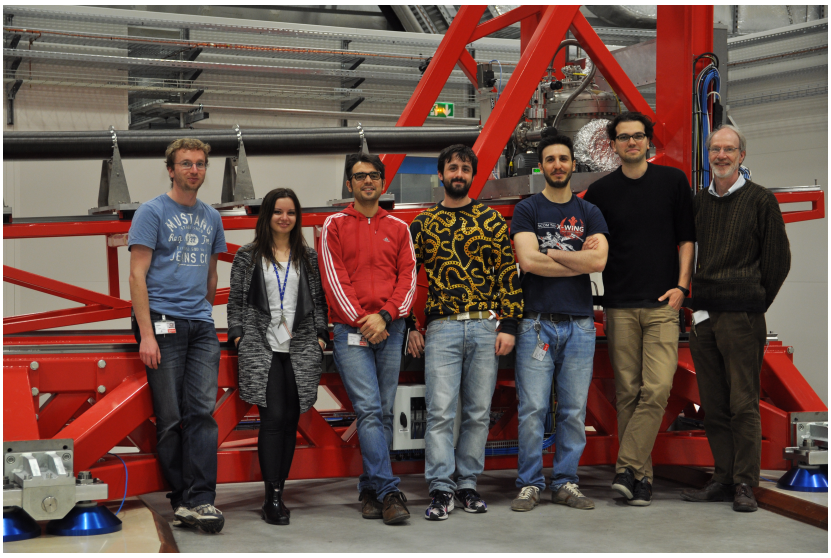

Figure 6: ID32 staff. From the left: Kurt Kummer, myself, Andrea Fondacaro, Andrea Amorese, Davide Betto, Emilio Velez-Fort, Nick Brookes.

presence by my side everyday. I love you girls!

To Josy, the best friend that any woman could wish for. We are not afraid of the distance between us, we are stronger.

To Elisa and Ilenia, thanks for encouraging and helping me in the most difficult choices and moments. To my classmates: Andrea, Giulia, Martina, Carlo, Luca, Gian, Nicola, Tobia, Matteo, Alessandro Bric, Alice, Riccardo. In one way or another, they all have been precious friends during these five years and I hope this will also continue out of the university.

To the other adventurers, like me, in Grenoble: Anastasia, Ruggero, Alessando, Andrea.

Thanks to the "Bar Doppio Senso" staff, Giampiero and Antonio, for having brightened my stressful evenings with chips and beer.

Thanks to Roberto, always present during all these years, so precious to me. I will never forget the best and the worst periods spent together. Thanks for your patience with me, every day, since the beginning of this hard but beautiful journey. But remember, even if you will get a better mark, I'm

smarter than you anyway!! :-)
Furthermore, I want to thank my big family: my grandparents, my uncles, my aunts and all my cousins. Their love gives me the strength to overcome all the obstacles of life. Thanks also to two people that are now like a part of the family, Manolo and Francesca.
Thanks to my brother, Angelo, for all the quarrels we had and for all the times we made peace.
And finally, I want to express my gratitude to my parents, Michela and Francesco. No words would be suitable to describe how special they are and what they have done for me. Thanks for offering me a lot of opportunities and always being by my side.
To conclude, just few lines of a song, that summarize all my acknowledgments:

"*Quando vedo crollare quello in cui credo*
Poi mi sollevo riparto da zero
E so che ogni cosa la devo
Alle palle quadre di mio padre
Al suo sudore
Al sorriso di mia madre al viso di ogni nonno che proietta amore
A mio fratello piccolo ora più alto di me
e nonno mi protegge sulla stella più bella che c'è
E ai miei amici esauriti
Alle notti felici di vizi proibiti realizzi che lo stile è quando siamo uniti
Solo quando stiamo assieme
La storia è vivibile
Passa parola a ogni persona visibile
Tutto è possibile
Per chi non si arrende e difende il sogno che ha
Mentre il sole che scende saluterà..."

"Gente che spera", Articolo 31

Bibliography

[1] L. J. P. Ament, M. Van Veenendaal, T. P. Devereaux, J. P. Hill, and J. Van Den Brink, Reviews of Modern Physics **83**, 705 (2011), arXiv:1009.3630 .

[2] L. J. P. Ament, G. Ghiringhelli, M. M. Sala, L. Braicovich, and J. van den Brink, Phys. Rev. Lett. **103**, 117003 (2009).

[3] P. Glatzel, M. Sikora, and M. Fernández-García, The European Physical Journal Special Topics **169**, 207 (2009).

[4] S. G. Chiuzbăian, G. Ghiringhelli, C. Dallera, M. Grioni, P. Amann, X. Wang, L. Braicovich, and L. Patthey, Phys. Rev. Lett. **95**, 197402 (2005).

[5] A. Kotani and S. Shin, Rev. Mod. Phys. **73**, 203 (2001).

[6] G. Ghiringhelli, N. B. Brookes, E. Annese, H. Berger, C. Dallera, M. Grioni, L. Perfetti, A. Tagliaferri, and L. Braicovich, Physical Review Letters **92**, 117406 (2004).

[7] J. Zaanen, G. A. Sawatzky, and J. W. Allen, Phys. Rev. Lett. **55**, 418 (1985).

[8] L. Braicovich, J. van den Brink, V. Bisogni, M. M. Sala, L. J. P. Ament, N. B. Brookes, G. M. De Luca, M. Salluzzo, T. Schmitt, V. N. Strocov, and G. Ghiringhelli, Phys. Rev. Lett. **104**, 077002 (2010).

[9] H. Yavas, M. van Veenendaal, J. van den Brink, L. J. P. Ament, A. Alatas, B. M. Leu, M.-O. Apostu, N. Wizent, G. Behr, W. Sturhahn, H. Sinn, and E. E. Alp, Journal of Physics: Condensed Matter **22**, 485601 (2010).

[10] M. Minola, *Magnetic , Orbital and Charge Fluctuations in Layered Cuprates Studied By Resonant Soft X-Ray Scattering* (2013).

[11] G. Ghiringhelli, M. Matsubara, C. Dallera, F. Fracassi, R. Gusmeroli, A. Piazzalunga, A. Tagliaferri, N. B. Brookes, A. Kotani, and L. Braicovich, Journal of Physics: Condensed Matter **17**, 5397 (2005).

[12] A. Amorese, *Single Photon acquisition in CCD detectors for high resolution Resonant Inelastic Soft X-ray Scattering* (2013).

[13] "What is a synchrotron ?" .

[14] "How does a synchrotron produce synchrotron light?" .

[15] A. Hofmann, *The Physics of Synchrotron Radiation*, Cambridge Monographs on Particle Physics, Nuclear Physics and Cosmology (Cambridge University Press, 2004).

[16] D. Attwood, *Soft X-Rays and Extreme Ultraviolet Radiation: Principles and Applications* (Cambridge University Press, 2007).

[17] G. Ghiringhelli, A. Piazzalunga, C. Dallera, G. Trezzi, L. Braicovich, T. Schmitt, V. N. Strocov, R. Betemps, L. Patthey, X. Wang, and M. Grioni, Review of Scientific Instruments **77**, 113108 (2006).

[18] C. Langini, *Advances in the detection at the new XMCD and RIXS beamline of the ESRF* (2014).

[19] A. Amorese, G. Dellea, L. Braicovich, and G. Ghiringhelli, eprint arXiv:1410.1587 (2014), arXiv:arXiv:1410.1587v1 .

[20] G. Ghiringhelli, M. Matsubara, C. Dallera, F. Fracassi, A. Tagliaferri, N. B. Brookes, A. Kotani, and L. Braicovich, Physical Review B **73**, 035111 (2006).

[21] G. Ghiringhelli, A. Piazzalunga, C. Dallera, T. Schmitt, V. N. Strocov, J. Schlappa, L. Patthey, X. Wang, H. Berger, and M. Grioni, Physical Review Letters **102**, 2 (2009).

[22] C. e. a. Dallera, Physical Review B 56.3 1279 (1997).

[23] G. Dellea, *COLLECTIVE EXCITATIONS IN HIGH TEMPERATURE SUPERCONDUCTING CUPRATES STUDIED BY RESONANT INELASTIC SOFT X-RAY SCATTERING* (2016).

[24] M. E. Dinardo, A. Piazzalunga, L. Braicovich, V. Bisogni, C. Dallera, K. Giarda, M. Marcon, A. Tagliaferri, and G. Ghiringhelli, Nuclear Instruments and Methods in Physics Research, Section A: Accelerators, Spectrometers, Detectors and Associated Equipment **570**, 176 (2007).

[25] G. G. Pavlov and J. A. Nousek, Nuclear Instruments and Methods in Physics Research, Section A: Accelerators, Spectrometers, Detectors and Associated Equipment **428**, 348 (1999).

[26] K. Kummer and A. Tamborrino, " RIXSToolbox ," (2016).

[27] " Huber Loss function ," ().

[28] " Huber Loss Python examples ," ().

[29] G. Kotliar and D. Vollhardt, Physics Today **57**, 53 (2004).

[30] M. T. Hutchings and E. J. Samuelsen, Phys. Rev. B **6**, 3447 (1972).

[31] K. Arai, T. Okuda, A. Tanaka, M. Kotsugi, K. Fukumoto, T. Ohkochi, T. Nakamura, T. Matsushita, T. Muro, M. Oura, Y. Senba, H. Ohashi, A. Kakizaki, C. Mitsumata, and T. Kinoshita, Physical Review B - Condensed Matter and Materials Physics **85** (2012), 10.1103/PhysRevB.85.104418.

[32] M. Matsubara, T. Uozumi, A. Kotani, and J. C. Parlebas, Journal of the Physical Society of Japan **74**, 2052 (2005).

[33] H. Ishii, Y. Ishiwata, R. Eguchi, Y. Harada, M. Watanabe, A. Chainani, and S. Shin, Journal of the Physical Society of Japan **70**, 1813 (2001).

[34] M. Magnuson, S. M. Butorin, A. Agui, and J. Nordgren, Journal of Physics: Condensed Matter **14**, 3669 (2002), arXiv:/arxiv.org/abs/1201.0661 [http:] .

[35] F. M. F. de Groot, P. Kuiper, and G. A. Sawatzky, Phys. Rev. B **57**, 14584 (1998).

[36] S. Huotari, F. Albergamo, G. Vanko, R. Verbeni, and G. Monaco, Review of Scientific Instruments **77**, 053102 (2006), http://dx.doi.org/10.1063/1.2198805.

[37] G. Ghiringhelli, A. Piazzalunga, C. Dallera, G. Trezzi, L. Braicovich, T. Schmitt, V. N. Strocov, R. Betemps, L. Patthey, X. Wang, and M. Grioni, Review of Scientific Instruments **77**, 1 (2006).

[38] J. P. Hill, G. Blumberg, Y.-J. Kim, D. S. Ellis, S. Wakimoto, R. J. Birgeneau, S. Komiya, Y. Ando, B. Liang, R. L. Greene, D. Casa, and T. Gog, Phys. Rev. Lett. **100**, 097001 (2008).